Applied Materials Today 36 (2024) 102053

Contents lists available at ScienceDirect

Applied Materials Today

journal homepage: www.elsevier.com/locate/apmt

An overview of advanced oxidation processes using copper-based catalytic degradation of organic pollutants in water

Enyioma C. Okpara [a,*], Olanrewaju B. Wojuola [a], Taiwo W. Quadri [b,c], Craig E. Banks [d,*]

[a] Department of Physics, Faculty of Natural and Agricultural Sciences, North-West University (Mafikeng Campus), Private Bag, X2046, Mmabatho 2735, South Africa
[b] Centre for Materials Science, College of Science, Engineering and Technology, University of South Africa, Johannesburg 1710, South Africa
[c] Institute for Nanotechnology and Water Sustainability, College of Science, Engineering and Technology, University of South Africa, Johannesburg 1710, South Africa
[d] Faculty of Science and Engineering, Manchester Metropolitan University, Manchester, Chester Street, M1 5GD, United Kingdom

ARTICLE INFO

Keywords:
advanced oxidation processes
copper-based catalysts
photocatalysis
organic pollutants
water

ABSTRACT

Organic pollutants are harmful to the environment due to their bio-accumulative and long-persistent nature, causing adverse effects on plants, animals, and humans. Their rapid spread beyond target applications in the ecosystem could be responsible for various fatal diseases and eco imbalances. Conventional techniques for removing these pollutants are ineffective because of their high solubility in water and nonbiodegradability. In contemporary times, we have witnessed a notable surge in interest in advanced oxidation processes (AOPs) for water treatment processes. This heightened attention is attributed to their exceptional degradation efficiency for recalcitrant organic pollutants. This review, therefore, focuses on copper-based homogeneous and heterogeneous catalysts for AOPs that offer both cost-effectiveness and high performance. Emphasis is placed on the use of copper-based catalysts in photocatalysis, Fenton-like process (including photo-Fenton (Fe^{2+}/UV/H_2O_2)), persulfates activation, and ultrasonic irradiation. The catalytic performance, mechanism, and pathway for the abatement of the target pollutants by the copper-based catalysts in each AOP are described in detail. The reusability, stability, and factors affecting the AOPs are briefly highlighted. We further provide perspectives on the key opportunities and challenges associated with copper-based catalysts in AOPs, recommending further exploration for enhanced applications in future studies.

1. Introduction

The rapid growth witnessed in population and industrialization has led to a significant global challenge – the contamination of water with organic pollutants. This issue poses a critical threat to public health and safety [1–4]. Wastewaters release various refractory organic compounds, including pharmaceuticals and personal care products (PPCPs), dyes, pesticides, and pharmaceuticals, into freshwater bodies [5–10]. It is recognised that these compounds are mostly persistent organic pollutants (POPs), which pose various threats to living organisms and humans [11–15]. Various biological and physical treatment techniques have emerged to address the elimination of organic contaminants from water, including methods such as coagulation, ultrafiltration, and adsorption [16–23]. Nevertheless, the implementation of these in practical scenarios are often set back by inefficient removal of trace organic pollutants resulting from the phase transfer of organic pollutants.

Additionally, there is a possibility of generating toxic by-products and wastes that could cause secondary pollution. Therefore, economic, eco-friendly, and highly effective treatment processes have become crucial for the removal of POPs in water. The advanced oxidation processes (AOPs) have fuelled great interest among researchers globally, sequel to their high efficacy in the degradation and even mineralization of aqueous organic pollutants [24-27,28]. Moreover, the AOPs demonstrate greater eco-friendliness compared to biological and physical treatment methods, as they involve reduced sludge generation or do not require diversion of organic pollutants from one phase to the other [29–31]. The AOPs support the degradation and mineralization of most organic pollutants into intermediate H_2O, CO_2, or other smaller intermediate products [32]. The unique activity and adaptability of the AOPs are incident on the generation of highly reactive oxygen species (ROS) such as $O_2^{\bullet-}$, $^1O_2$, $SO_4^{\bullet-}$, and $^\bullet OH$, which effectively attack the organic pollutants resulting in their decomposition [33–35].

In general, numerous AOPs exist, including photochemical

* Corresponding authors: Enyioma C. Okpara, and Craig E. Banks
E-mail addresses: 29938155@mynwu.ac.za (E.C. Okpara), c.banks@mmu.ac.uk (C.E. Banks).

https://doi.org/10.1016/j.apmt.2023.102053
Received 1 December 2023; Received in revised form 22 December 2023; Accepted 30 December 2023
Available online 13 January 2024

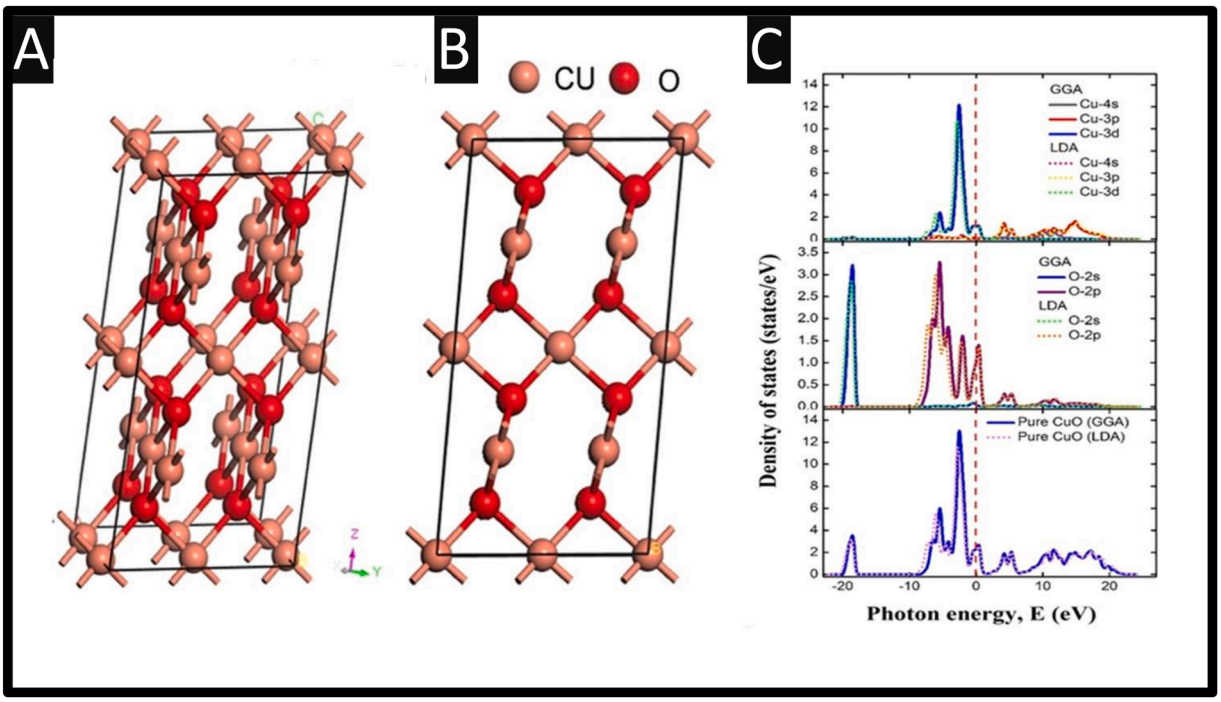

Fig. 1. The crystal structure of (A) 3D CuO and (B) 2D CuO and (C) the partial and total density of states (DOS) of CuO supercell. Figure reproduced from reference [47]. Copyright 2020 Elsevier.

oxidation, ozone oxidation, electrochemical oxidation, Fenton and Fenton-like oxidation [36]. Typically, AOPs consist of homogeneous AOPs (homAOPs) and heterogeneous AOPs (hetAOPs). The hetAOPs commonly employ solid in conjunction with other systems (light, ozone (O_3), persulfates (PS), H_2O_2, Cl^-, etc) to decompose organic contaminants [37–39]. Relative to the homAOPs catalysts, the primary benefit of their heterogeneous counterparts lies in the ease of recovering and reusing the catalyst. In real-world water treatment applications, it is expected that heterogeneous catalysts meet certain criteria, including chemical and physical stability, as well as sustainability [32]. Consequently, various endeavours have been dedicated to the exploration of durable and efficient heterogenous catalysts for AOPs with particular emphasis on copper-based catalysts (CBC). Copper (Cu) has been recognised as an efficient activator for initiating AOPs, leading to the generation of strong oxidants. Given the presence of Cu ions in many water/wastewater samples, exploring CBC holds potential for water remediation. In this review, we summarise the use of copper-based catalytic degradation of organic pollutants in water using AOPs, reporting on opportunities and challenges with emphasis on enhanced applications for researchers to pursue.

2. Copper-based catalysts for AOPs

Copper-based catalysts (CBC) have in recent years emerged as auspicious catalysts in AOPs owing to their earth abundance, easy preparation, minimal toxicity, good stability, cost-effectiveness, and unique electronic configurations. A variety of CBC have been synthesized and applied in AOPs to efficiently degrade and mineralize organic pollutants in water with high efficiency, reusability, stability, and low toxicity of intermediate products.

2.1. *CuO/Cu_2O homogeneous structures in AOPs*

Cupric oxide has piqued research interest due to its unique characteristics as a p-type semiconductor featuring a narrow band gap (1.2-2.0 eV). It serves as the basis for huge magnetoresistance and finds application in numerous high-temperature semiconductor devices [40,41]. Cupric oxide monoclinic crystal architecture, Fig. 1, exhibits exceptional chemical and physical properties such as favourable electrochemical performance, appropriate redox potential, super thermal conductivity, exceptional stability in solution and large surface area [42,43]. CuO is made up of 3d and O 2p shells occupied by conduction band (CB) and valence band (VB) edges having lower energy gap (E_g) leading to the optimal generation of ROS. Additionally, its visible light (VL) wavelength of maximum absorbance (λ_{max}) extends up to the infrared region [44,45]. For instance, a CuO photocatalyst with an E_g of 1.7 eV has a CB of 0.46 V and a VB of 2.16 V potential, which represents a potential greater than the standard redox potential and appropriate also for $^{\bullet}OH$ and $O_2^{\bullet-}$ radical release, needed for photodegradation [46].

2.2. *Cu-O based heterostructures in AOPs*

Pure CuO transition metal oxides are not very effective in degrading organic pollutants because of rapid charge recombination in photocatalysis, and sluggish Cu^+/Cu^{2+} redox cycle in Fenton-like process and PS activation. Consequently, numerous strategies are required to augment the catalytic efficiency, improve stability, and achieve recyclability. These strategies include doping with transition and rare earth metals, constructing binary, ternary, and even quaternary heterojunctions, forming Z-scheme heterojunctions, and incorporating carbonaceous materials [48].

2.3. *Cu-S based heterostructures in AOPs*

Generally, transition metal sulfides (TMS) are some of the most abundant and widely distributed semiconductor materials on Earth. In these materials, a combination of sulfur anion with a metal/semi metal cation occurs leading to the formation of M_xS_y compounds with diverse stoichiometries [49] or bimetallic sulfides described as $A_{1-x}B_xS_y$ (A and B representing different metals, while x and y are integers) [50,51]. Contrary to other popular transition metal catalysts, the TMS exhibit rich redox sites, higher electrical conductivity, superior optical properties, a tuneable band gap, excellent thermal and mechanical stabilities, in addition to high catalytic activity [52,53]. For instance, a 2D $CuCo_2S_4$

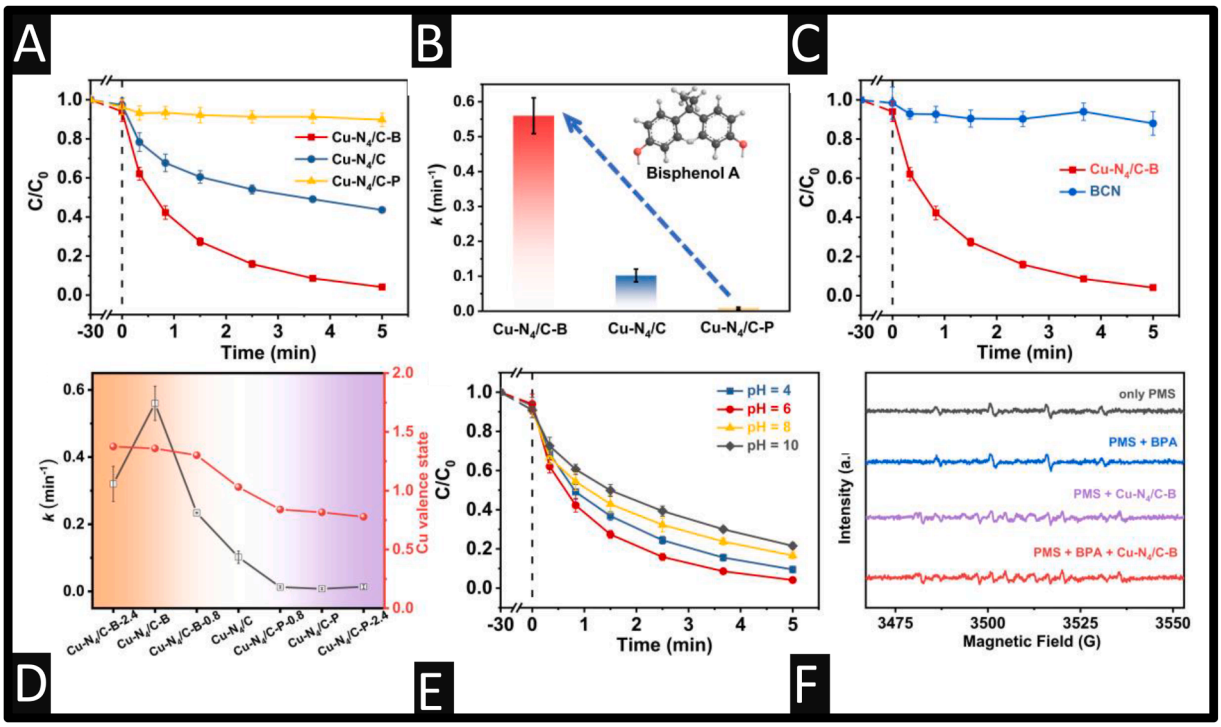

Fig. 2. Fenton-like activity of Cu-N_4 catalysts. (A) Kinetics of the bisphenol A (BPA) degradation in Cu-N_4/C-B/PMS system, Cu-N_4/C/PMS system, and Cu-N_4/C-P/PMS within 5 mins. (B) Comparing the *k* value of BPA decomposition using different Cu-N_4 catalysts. (C) Kinetics of BPA degradation in Cu-N_4/C-B/PMS system and BCN/PMS system. (D) The relationship between *k* and the Cu valence state in the as-prepared Cu-N_4 catalysts. (E) Effect of pH on BPA degradation in the Cu-N_4/C-B/PMS system. (F) EPR spectra of the PMS activation in the presence of Cu-N_4/C-B catalyst. (Reaction condition: [BPA] 20 ppm, [PMS] 200 ppm, [catalyst] 100 ppm, T = 298 K, $[pH]_0$ = 6.0. Figure reproduced from reference [57] Copyright 2022 National Academy of Sciences.

nanosheet (E_g = 2.24 eV) facilitated the generation of a well-opened 3D hierarchical structure, exposing greater portion of the surface. As a result, the nanosheet was enriched with capacities to absorb the whole visible light spectrum for water splitting reactions, with probable apparent quantum yield reaching 2.48%. The indirect band gap of the nanosheet limited the rapid recombination of charges. In addition, the $CuCo_2S_4$ nanosheet possessed a high surface area of 62.9 $m^2\ g^{-1}$ and donor concentration of $7.22 \times 10^{18}\ cm^{-3}$ alongside a richly filled DOS at the Fermi level, which supports H^+ adsorption on S-sites, thus making it a promising photocatalyst [54].

2.4. Cu-N_x heterostructures in AOPs

Developing hetAOPs with atomically dispersed active sites is crucial to enhance oxidant activation in Fenton-like processes. However, effectively manipulating the electronic configuration of metal centres to boost the activation kinetics is still difficult. Recent research has shown that the abundance of Cu-N_x species demonstrates the potential to enhance the decomposition of H_2O_2 to generate $^{\bullet}OH$ radicals [55]. However, decorating g-C_3N_4 with metals in the form of single-atoms and ultra-small clusters has emerged as a hot research area due to the exceptional performance of high atom-utilization [56]. Zhou *et al.* [57] successfully configured the electronic structure of Cu-N_4 sites by incorporating electron-deficient Boron (B) or electron-rich phosphorous (P) into a carbon substrate towards the activation of peroxymonosulfate (PMS) in a Fenton-like reaction. Interestingly, the electron-deficient Cu-N_4/C-B presented the most active oxidation activity than Cu-N_4/C-P and Cu-N_4/C (Fig. 2). In contrast, Cu-N_4/C-P decreased PMS activation, attributed to the decrease in the electronic density of active sites of Cu, and the downshifts of the d-band centre due to long interaction with B atoms. Thus, this increased the energy of absorption required for the activation of PMS.

2.5. Cu-C heterojunction in AOPs

Cu metal has been used to dope carbonaceous materials and increase the quantity of active sites contained in the carbon material. This involves the formation of Cu-C sites that boost the interaction with PS. For example, Yu and co-workers [58] fabricated a Cu-doped sludge biochar (CSBC) by simple impregnation-pyrolysis technique. The loaded Cu^{2+} in the sewage sludge was transformed into Cu^0/Cu^I species following pyrolysis, which significantly amplified the removal efficiency of bisphenol A (BPA) and increased the pH window.

2.6. Copper metal oxides (Cu-MO) heterostructure in AOPs

Copper metal oxides (Cu-MO) exist in two different forms, cupric oxide (CuO) and cuprous oxide (Cu_2O). To ensure the total oxidation of pollutants while minimizing the quantity of leached active metal into the solution, it is imperative to optimize reaction conditions such as oxidant concentration (H_2O_2, PDS, etc.,), catalyst loading, and pH [59]. For a Fenton-like process, Fang *et al.* reported that the use of pure CuO nanosheets revealed that a concentration of 20.3, 13.6 and 10.5 ppm Cu leached into the solution at pH levels of 3, 6 and 9, respectively [60]. A similar observation was made in a CuO/CeO_2 heterostructure, where 9% of the Cu loading leached into the solution at pH 5, which limited the reusability of the catalyst [61]. However, doping metal oxide semiconductors with Cu reduced the leaching of the Cu metal into the solution. Silva *et al.* [62] demonstrated the effectiveness of Cu-MgO nanoparticles (NPs) in Fenton-like catalysis for the degradation of pharmaceutical pollutants in wastewater. Under ideal circumstances, they achieved complete oxidation of salicyclic acid (SAA) within 60 mins. The dissolution of MgO at the surface led to an increase in the pH of the solution, which completely prevented the leaching out of Cu, while maintaining high catalytic performance. Note that even after five cycles, the catalyst's reusability remained satisfactory.

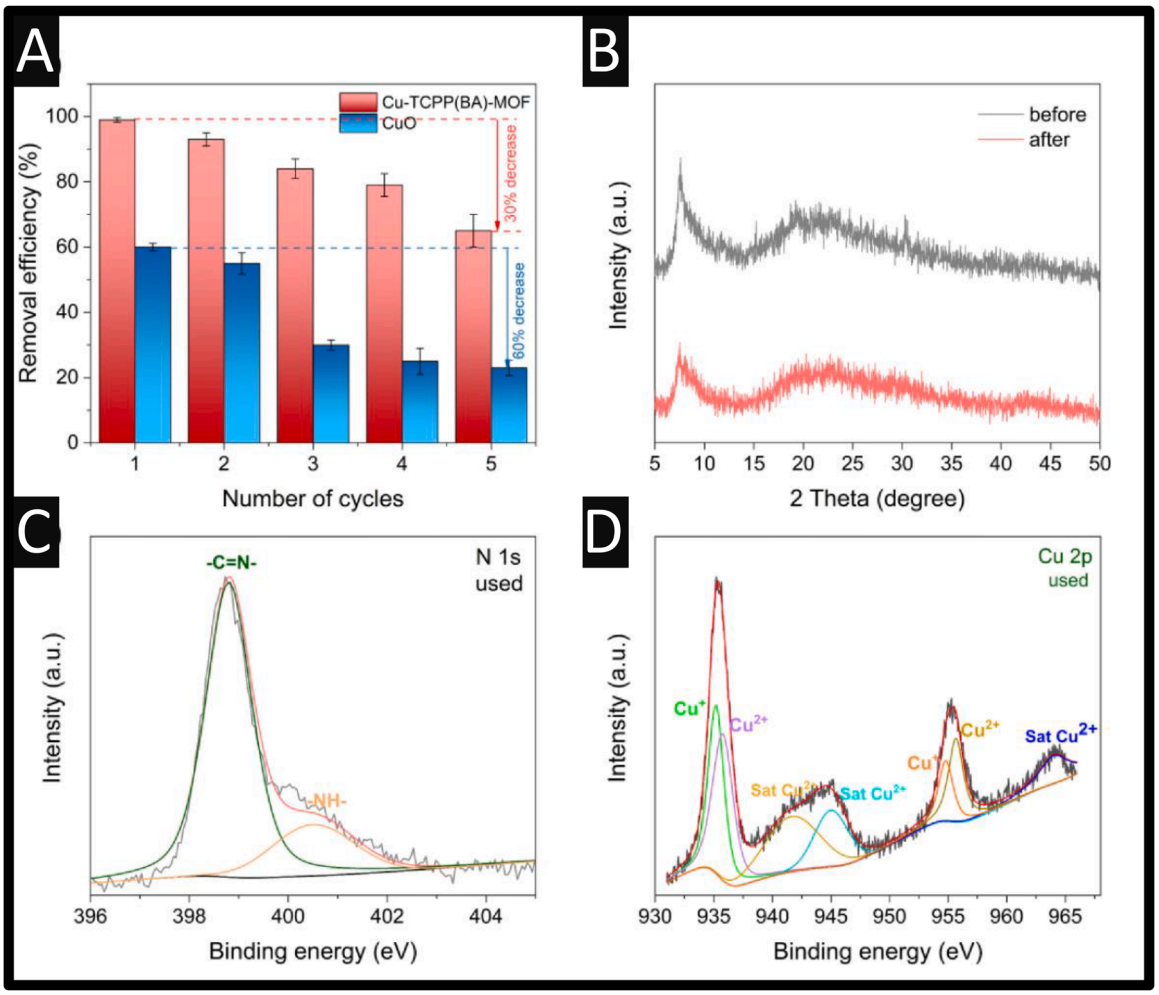

Fig. 3. **A:** Cu-TCPP(BA)-MOF and stability activity test of CuO; **B:** Comparing the XRD pattern of the applied catalyst and fresh catalyst; **C:** XPS spectra N1s of applied Cu-TCPP(BA)-MOF; **D:** XPS Cu 2p spectra of applied Cu-TCPP(BA)-MOF. Figure reproduced from reference [67]. Copyright 2022 Elsevier.

2.7. Copper metal organic frameworks (Cu-MOF) heterostructures in AOPs

In recent years, metal-organic frameworks (MOF) have attracted huge development potential due to their distinctive structural features such as large specific surface area (SSA), adjustable structure and high porosity [63]. They have seen notable advances in modern material science. Additionally, the arrangements of organic ligands, clusters, or metal ions provide a pellucid directionality in MOFs to generate diverse framework pore structures, resulting in different adsorption [64], optical [65], and electromagnetic [66] properties. Bai *et al.* [67] employed Cu porphyrin and Cu as ligand and metal node, respectively, in designing an ultra-thin MOF enriched with Cu^{2+} active sites for the degradation of refractory rhodamine B (RhB) in water, in a PMS system. The Cu-modified MOF exhibited superior catalytic removal efficiency, and lower ion leaching compared to pure CuO in the degradation of RhB (Fig. 3).

2.8. Zero valent copper

Zero valent copper systems are promising in the area of environmental remediation and have been used with ultrasonic irradiation to activate oxidants for various applications. For instance, it has been used with PS for the degradation of bisphenol AF, [68] H_2O_2 for the oxidative degradation of norfloxacin, [69] and for acetaminophen (ACT) [70]. A further report suggests that the injection of Cl^- significantly enhances the remediation of ACT, where the generation of $^{\bullet}OH$ and reactive chlorine species is attributed to play dominant roles [71]. Other approaches have used zero valent copper to activate PS via ultrasound for the degradation of p-chlorophenol [72].

2.9. Copper layered double hydroxide (Cu-LDH)

Layered double hydroxides as catalysts for AOPs have been extensively studied. The use of Cu-LDH involves layer structures that can be tuned in terms of morphology, composition, surface defect structure and particle size through various synthetic methods and exfoliation approaches. This allows for the creation of low-coordinated steps, edges, and/or corner atoms, which facilitate heterogeneous catalysis. Moreover, strong electrostatic interactions between layers and interlayer anions contribute to an ordered arrangement of interlayer species and an orientation of active sites [27]. For example, Cu-Co-Fe-LDH was synthesized to activate PMS for nitrobenzene (NB) degradation, resulting in the generation of $^{\bullet}OH$ and achieving the degradation of 16 μM in 6 mins [73]. Another notable work has reported the use of LDH-MoS_4 with Cu (II) ions in conjunction with PS to improve the efficiency by 10-20 times in the removal of atrazine (ATZ) over that of previously related structures, where the authors report that the role of Cu(II) ions are continuously supplying electrons from the unsaturated S^{2-} and Mo^{4+} of the LDH-MoS_4 [74].

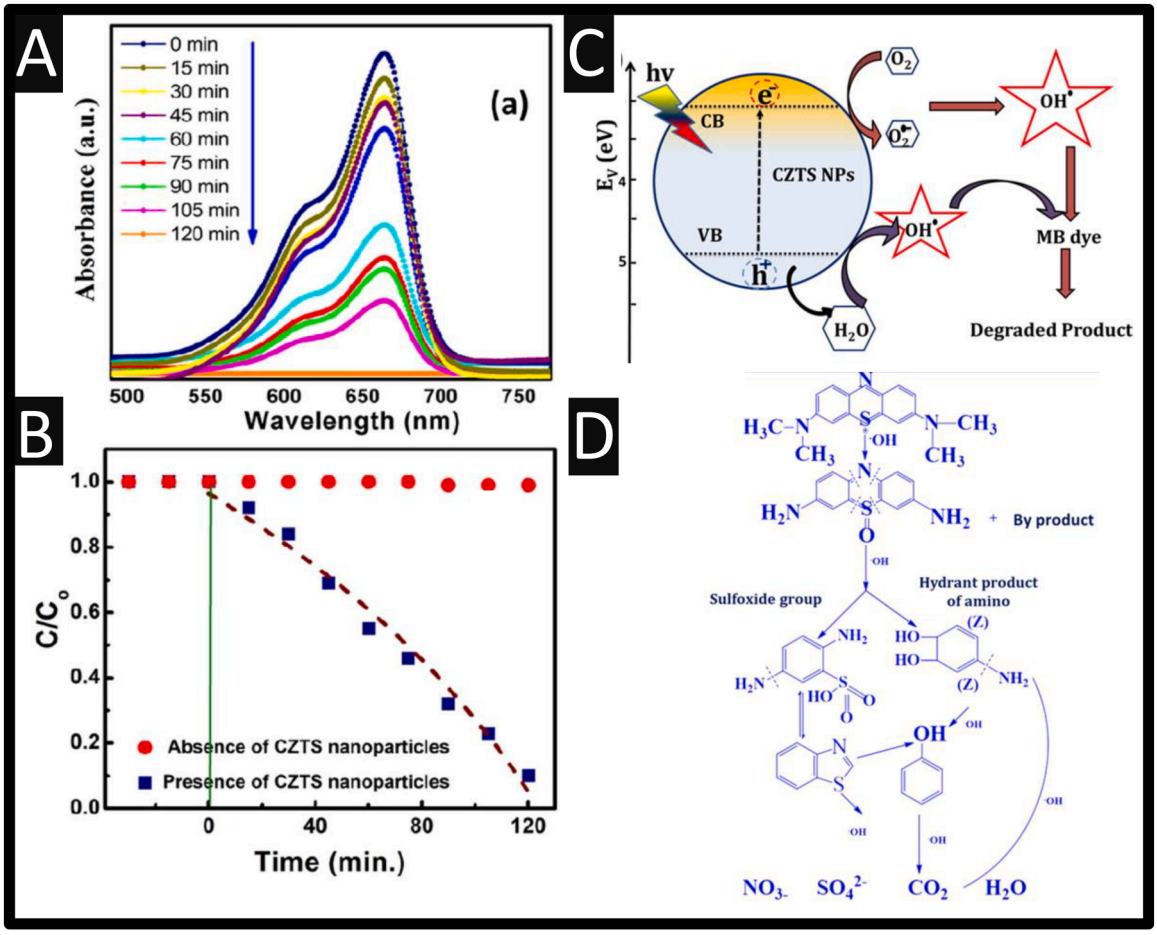

Fig. 4. A: The UV-vis spectrum of the degraded pollutant, **B:** comparison between the kinetics in the presence and absence of the catalyst, **C:** the schematic representation of energy level diagram revealing the band structure and separation of h^+ and e^- at the catalyst interface and **D:** the mechanism of the degradation of MB. Figure reproduced from reference [88]. Copyright 2017 Elsevier.

3. Application of copper-based catalysts in AOPs

3.1. Photocatalysis

Photocatalysis is an environmentally benign, sustainable, and energy-saving technology that utilizes solar energy to degrade organic pollutants. With the advent of semiconductor-based photoelectrochemical water-splitting reactions, photocatalysis, as an AOP has attracted huge research attention in recent years. It has gained wide applications in the degradation of contaminants characterized with low biodegradation, high complexity and high concentration [75]. Furthermore, there is an increasing usage of metal oxides such as TiO_2 and ZnO as semiconductor photocatalysts, for the generation of photoinduced electron (e^-) and hole (h^+) that react with the ^-OH group, O_2, and H_2O to form ROS, such as hydroxyl radical ($^•OH$) and superoxide radical anion ($O_2^{•-}$) with strong oxidation activities [52,76–78]. In a typical photocatalysis, when a light with the appropriate wavelength (adequate energy) falls on a photocatalyst, the photon energy is absorbed by a VB e^-, and it is excited to the CB. Herein, a h^+ is generated in the VB. The outcome of this process is the generation of photoexcitation, and e^- and h^+ pair. The excited electron is employed in the reduction of an acceptor in which a h^+ is utilised for oxidation of donor molecules where the fate of e^- and h^+ is determined by the relative positions of the valence and conduction bands in a semiconductor system and the redox substrate levels [79]. Based on band gap, materials are divided into three main types: *insulator, conductor and semi-conductor*. Therefore, the applicability of photocatalysis in the abatement of organic contaminants in water could be limited by high E_g, rapid recombination rates of the photoinduced e^- and h^+, and weak light absorption capacities [80,81]. Large E_g values necessitate the absorption of more light (energies) to reach the separation of charge carriers [82]. In addition, the e^- and h^+ can easily recombine without taking part in the reaction. This spontaneous e^--h^+ recombination can result in reduced amount of photoinduced ROS present on reaction sites to undergo photoreduction.

Since most semiconductor metal oxides used in photocatalysis have high E_g values, several research directions have shifted towards modification of photocatalysts to overcome the limitations concomitant to their applications in photocatalysis. The evaluation of different hybrid nanocomposites for their lower E_g values [83], tuneable morphology [84,85], and reduced charge recombination capacities have been conducted [86]. With regards to degradation of organic contaminants via photocatalysis, Cu-based nanomaterials have demonstrated appreciable catalytic properties on account of their good stability and reusability [87]. For example, Ansari *et al.* [88], fabricated a low-cost single phase quaternary semiconducting copper zinc tin sulfide (Cu_2ZnSnS_4) NPs, with low band gap (1.72 eV), and a high degree of absorption coefficient ($\sim 10^4$ cm^{-1}) for a VL irradiation of methylene blue (MB) dye. A total decomposition of the MB dye was realized in 120 mins with small amount of the catalyst (Fig. 4A,B). Empirical data obtained in the study aligned with a pseudo-first order kinetics with a rate constant (k) value of 0.0144 min^{-1}. The exceptional performance observed in the degradation of the MB was attributed to small and uniform distribution size of the Cu_2ZnSnS_4 NPs ($\sim$ 7 nm), and even dispersion without agglomeration; the photocatalysis and mechanism of the degradation is

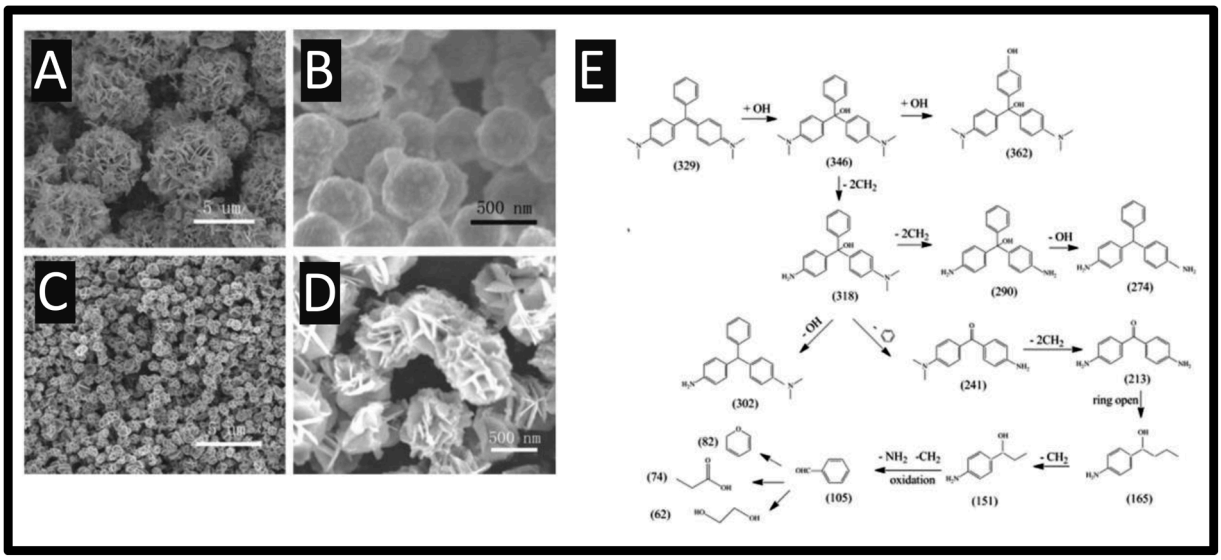

Fig. 5. Morphological characterizations of Cu_2CdSnS_4 nanoflowers (**A-D**), mechanistic pathway of the degradation of MG using Cu_2CdSnS_4 nanoflowers (**E**). Figure reproduced from reference [93]. Copyright 2022 Elsevier.

schematically represented in Fig. 4C and D.

From equation 1, the irradiation of the VL (from 0. 15 kW halogen lamp) with $h\nu > E_g$ on the catalyst formed e^- and h^+ in the Cu_2ZnSnS_4 nano architecture, which acted as a strong redox agent.

$$Cu_2ZnSnS_4 + h\nu \rightarrow Cu_2ZnSnS_4 + h^+ + e^- \quad (1)$$

$$h^+ + H_2O \rightarrow OH^\bullet + H^+ \quad (2)$$

$$O_2 + e^- \rightarrow O_2^{\bullet -} \quad (3)$$

$$O_2^{\bullet -} + H^+ \rightarrow OOH^\bullet \quad (4)$$

$$2OOH^\bullet \rightarrow H_2O_2 \quad (5)$$

$$H_2O_2 \rightarrow 2OH^\bullet \quad (6)$$

Consequently, water adhered onto the surface of Cu_2ZnSnS_4 NPs, enters the h^+, and is oxidized to form OH radical. The e^- at the CB was taken by the O_2, to form anionic $O_2^{\bullet -}$ radical, which partakes further in the oxidation activity. The $O_2^{\bullet -}$ radical reacts with H^+ to form $OOH^\bullet$ which generates H_2O_2 that subsequently turns into an aggressive $^\bullet OH$. The $^\bullet OH$ thus formed attacks the aromatic ring of the MB, ripping open the hydroxylated ring and azo bond to produce H_2O, CO_2, NO_3, NH_4^+ and SO_4^{-2} ions [89]. Other related works in the degradation of MB using quaternary Cu_2ZnSnS_4 were described in the one-step synthesis by Zhou *et al.* [90] and two-step synthesis by Phaltane *et al.* [91]. Quaternary Cu_2ZnSnS_4 (CZTS) thin films were also useful in their phase dependent photocatalytic degradation of RhB dyes [92] with the highest k value achieved in the pure phase.

To forestall Sn_{Cu} and Cu_{Sn} defects, achieve lower E_g value, reduce e^--h^+ recombination, enhance light absorption efficiency and increase the SSA and improve crystallinity, Xu and co-workers [93], substituted Zn with Cd in hierarchical Cu_2CdSnS_4 nanoflowers (Fig. 5A-D) for the irradiation of malachite green (MG). The degradation obeyed a pseudo-first-order kinetics ($k = 5.68 \times 10^{-3}$), and more than 90% degradation of MG was achieved in 120 mins. The mechanism (Fig. 5E) indicated that the degradation of MG originated from *N*-demethylation, elimination of benzene ring and subsequent ring-open reactions.

The synthesis and applications of magnetic and biocompatible NPs have become a popular part of the growing scientific explorations in modern times [94,95]. The use of magnetic compounds has become known as a competitive substitute to heterogenous catalysts due to their ease of separation [96–98]. Diverse compounds such as zeolites [99, 100], polysaccharides [101], lignin [102], magnetic compounds [103], and graphene [104] have been applied in the dispersion and prevention of agglomeration of metal NPs. The use of biological polymers has become common because of their environmental friendliness, accessibility, unique physical properties, and low cost of preparation [101, 102]. Lignin is the second most abundant biopolymer with active sites such as hydroxyl, carbonyl, aldehyde, phenolic and methoxy moieties [102] Herein, Orooji *et al.* [105], valorised lignosulfonate (sulfonic acid-based lignin) into a Cu-containing magnetically recyclable photocatalyst (FLN-Cu complex) for the degradation of Congo red (CR), RhB, and MB, depending on the reaction time, temperature and catalyst load. At optimal conditions, 95% of the MB was removed in 60 mins.

To further enhance the activity of CBC in the irradiation of organic pollutants, carbonaceous materials with high SSA (theoretical SSA of 2.63 $km^2\ kg^{-1}$) [106], excellent electronic attributes (mobility of charge carriers 20 $m^2\ V^{-1}\ s^{-1}$ at ambient temperature) [107], optical and mechanical characteristics (mechanical strength of 1.06 Tpa) [108–110] and thermal properties (thermal conductivity of 5.3 $kWm^{-1}\ K^{-1}$) [111] were conjugated with Cu. For example, the graphitized Cu–P25 (Cu–P25–graphene) nanocomposite was prepared by Jin *et al.* [112]. The synergistic impacts of Cu^{2+} ions and graphene not only enhanced better charge separation capacity but presented extended light absorption (by Ti−O−C bonds) in the VL and narrowed the band gap of TiO_2, which played a huge role in the degradation of MB. Benefiting from the charge separation, Cu–P25–graphene nanocomposite demonstrated high activity for MB degradation under VL irradiation, obtaining 98% within 100 mins. Copper in the composite behaves as the capture centre for the e^- that reduces the charge recombination rate. Consequently, the production of $O_2^{\bullet -}$ and $^\bullet OH$ radicals at the catalyst surface was amplified, which resulted in the faster abatement of the dye. Additionally, the excellent absorption ability of graphene boosted π-π driven complexation between the aromatic regions of graphene and MB [113]. Good stability of the designed catalyst is attributed to strong chemisorption on the surface of TiO_2 promoted by the interaction between P25 and graphene, making it difficult to be removed after 5 repeated cycles.

Rare earth-based copper oxide Ln_2CuO_4 (Ln = Eu, Tb, Sm, Pm, Nd, etc.) nanostructures are distinct for their unique attributes that position them for industrial relevance in applications such as magnetocaloric materials, sensors, and superconductors [114,115]. In recent years, this group of photocatalysts have gained extensive usage in photocatalysis. In one of such cases, Yousefzadeh *et al.* [116], synthesized a pure phase Sm_2CuO_4 nanostructures using the sonochemical approach (power 10%

Table 1
Reaction conditions and efficiencies of Cu-based catalysts as photocatalysts towards the removal of organic contaminants in water

Reaction conditions					Efficiency of catalyst				
Catalyst	Contaminant	[C]	[Cu]	Irradiation	E_g (eV)	[EoD] (min)	k (min^{-1})	KRS	Reference
Cu_2ZnSnS_4 NPs	MB	10 ppm	10 mg	0.15 kW THL	1.72	>99 % (120)	0.0144	$^{\bullet}OH$	[88]
Cu_2ZnSnS_4 NPs-H_2O_2	MB	10 ppm	20 g	0.1 kW XLS		100% (90)	0.04	$^{\bullet}OH$	[90]
Cu_2ZnSnS_4	RhB	-	-	VL	2.05 – 1.45	79% (240)	0.0065	$O_2^{\bullet-}$ and $^{\bullet}OH$	[119]
Cu_2ZnSnS_4	BB 41 AO 8			VL	1.90	90% (120)			[120]
Cu–P25–graphene	MB	10 ppm	100 mg	0.25 kW XLS	-	98% (100)	0.0387	$O_2^{\bullet-}$ and $^{\bullet}OH$	[112]
Cu_2ZnSnS_4	MB	70 ppm	25 mg	VL	1.53	50% (45)	0.018	$^{\bullet}OH$	[91]
CuO-NPs	MB	200 mg	0.005 M	VL	3.24	97% (50)	0.01	$^{\bullet}OH$	[121]
TiO_2/CuO	MO	-	-	6 W UV lamp	2.53	95% (210)	0.0151	$^{\bullet}OH$	
TiO_2/CuO/U/CN nanocomposite	DR 16	-	-	0.05 kW LED lamp	1.5	100% (120)	-	$^{\bullet}OH$, and $O_2^{\bullet-}$	[122]
CuO/$Cu(OH)_2$ nanostructure	RG 19A	50 ppm	200 mg/L	Vilber Lourmat Multilamp	2.39	98% (12)	0.0033	$^{\bullet}OH$ $O_2^{\bullet-}$ and h^+	[123]
CuO/Cu_2O	MO	20 μM	15 mg	0.3 kW XLS	-	90% (30)		$^{\bullet}OH$ and $O_2^{\bullet-}$	[124]
Nano TiO_2/CuO	MB	10 ppm	100 mg	0.3 kW XLS	-	99% (300)	-	$O_2^{\bullet-}$	[125]
Co_3O_4/CuO	MB	10 ppm	-	0.5 kW XLS	Co_3O_4= 1.7 CuO= 1.4	56% (180)	-	$^{\bullet}OH$ and $O_2^{\bullet-}$	[126]
ZnO/CuO	O-II	12 ppm	-	XLS	2.77	41.8% (300)	≈ 0.01	$^{\bullet}OH$ and $O_2^{\bullet-}$	[127]
ZnO/CuO	DB 71	20.34 ppm	1.85 g/L	Sunlight	-	89.58% (177.13)	-	$^{\bullet}OH$	[128]
N,Cu–TiO_2	MB	10 μM	-	Sunlight	-	> 95% (360)	0.007	$O_2^{\bullet-}$ and $^{\bullet}OH$	[129]
$CuCr_2O_4$/CuO	MO/MB	15 ppm	50 mg	0.3 kW XLS	1.23	97.16%/98.16%	0.01550/ 0.01161	$^{\bullet}OH$ and $O_2^{\bullet-}$	[130]
Chitosan/ZnO/CuO	FG	30 ppm	-	0.1 kW HPML	-	91.21% (110)	-	$^{\bullet}OH$ and $O_2^{\bullet-}$	[131]
Graphene/CuO NC	MB	20 ppm	0.3g/L	Sunlight	1.39 ± 0.09	99.44% (80)	0.06	$^{\bullet}OH$, $O_2^{\bullet-}$ and h^+	[132]
CuO/Cu_2O/Cu	MB	10 ppm	0.3 g/L	Blue LED lamp	1.42	91.91% (90)		$^{\bullet}OH$, $O_2^{\bullet-}$ and h^+	[133]
Fe_3O_4/rGO/CuO/H_2O_2	MB	30 ppm	10 mg	0.5 kW XLS	1.5	98.70% (150)	0.0175	$^{\bullet}OH$, $O_2^{\bullet-}$ and h^+	[134]
$BiVO_4$/CuO (e 0.75Cu/BVO)	BPA	210 ppb	0-1000 mg/L	0.1 kW XLS	2.30	95% (5)	-	$^{\bullet}OH$ and $CO_3^{\bullet-}$	[135]
ZnAl LDH/g-C_3N_4/CuO NPs	Phenol	20 ppm	1.0 g/L	0.125 kW UV lamp/VL	3.10	85% (60)	0.0330 /0.00083/h	$^{\bullet}OH$, and $O_2^{\bullet-}$	[136]
Fe_3O_4/CuO	p-ASA	133 ppb	10 mg	0.3 kW XLS	1.69	100% (32)	0.1056	$^{\bullet}OH$, and $O_2^{\bullet-}$	[137]
CuO-CP	PAP	20 ppm	2.0 g/L	-	-	≈ 60% (120)	0.0054	$^{\bullet}OH$	[138]
Ag_3PO_4/CuO	Phenol	-	-	0.125 kW, UV lamp	CuO-1.7; Ag_3PO_4-2.45	-	-	$^{\bullet}OH$	[139]
g-C_3N_4/CuO	RhB			0.3 kW XLS		100% (5)		$O_2^{\bullet-}$	[140]
WO_3/CdS/ CuO	MB	10 ppm	5 mg	0.3 kW Xe lamp	CuO-1.76, WO_3-2.87, CdS-2.33	87.11% (240)	-	e^- and h^+	[141]
CuS/Cu/CuO	MB	10 ppm		0.5 kW Xe lamp	1.63	98.6% (40)	0.1092	$^{\bullet}OH$	[142]
Pb_2O_3/CuO	RBD	-	-	0.3 kW Xe lamp	1.28	99% (90)	0.092	$^{\bullet}OH$ and $O_2^{\bullet-}$	[143]
Li_3BO_3/CuO	AV 7	10 ppm	50 mg	0.4 kW Osram lamp	3.11	80% (150)		$^{\bullet}OH$,	[144]
Li_3BO_3/Cu_2O					3.05	85% (150)	-	$O_2^{\bullet-}$ and h^+	
$Dy_2Cu_2O_5$	PR	10 ppm	100 mg	150 W VL	3.20	96.4% (120)	0.029	$^{\bullet}OH$	[145]
$Cu_3B_2O_6$	AV 7	25g/L	15 mg/L	GYZ-250	-	86% (90)	0.0182	$^-$	[146]
g-C_3N_4/$Cu_3B_2O_6$-H_2O_2	MB	10 mg/L	50 mg (60 wt. %)	300WXe-lamp	≈ 2.6	100% (60)	0.0474	$^{\bullet}OH$	[147]
Cu-WO_3	TC	50 mg/L	0.05 g	A 300 W Xe lamp	2.69	96.8%	-	$^{\bullet}OH$	[148]
$CuCo_2O_4$	AB 14 AR 88	25g/L	15 mg/L	250 W high pressure mercury lamp (GYZ-250)	1.74	79% (90) 89% (90)	0.0116 0.0159	$^{\bullet}OH$	[149]
$[Cu(SCN)_2(phen)_2]$ @CuI	AR 1	0.8 mM	1 g/dm^3	LED illuminator		>50% (60)	0.017.6	$O_2^{\bullet-}$	[150]
$La_2Cu_2O_5$	AB	10 ppm	30 mg	150 W VL	3.25	80.1% (120)	0.01332	$^{\bullet}OH$	[151]
Cu-ZnO/g-C_3N_4	ATZ	100 ppm.	0.5 g	VL	2.45	90% (120)	-	$^{\bullet}OH$, e^-, and h^+	[152]

(*continued on next page*)

Table 1 (*continued*)

Reaction conditions					Efficiency of catalyst				
Catalyst	Contaminant	[C]	[Cu]	Irradiation	E_g (eV)	[EoD] (min)	k (min^{-1})	KRS	Reference
3D NP-Cu+H_2O_2	MO, CR, MB, AO II and RhB	20 mg/L	27.2 g/L	Fluorescent lamp	2.0–2.2 eV	100% (10) (MO)	0.147	$^{\bullet}OH$	[153]
$Lu_2Cu_2O_5/Lu_2O_3$	TB	10 ppm	50 mg	400 W mercury lamp	3.20	98.5% (120)		$^{\bullet}OH$	[154]
RGO/Cu	RhB and MB	10 ppm			2.85	RhB = 91.0% (60) and MB = 72.0% (60)	RhB = 0.0409 MB = 0.0221	$^{\bullet}OH$ or $O_2^{\bullet-}$	[155]
CuO/C	MO and MV	1 μM	15 mg	Mercury lamp	~ 3.5	MV = 100% (10) MO = 100% (15)	-	$^{\bullet}OH$	[156]
TNCuPc	RhB	10 mg/L	0.05 g	0.15 kW xenon lamp	-	91% (300)	-	$^{\bullet}OH$	[157]
ZnO/CuO (8:1)/Pd	RhB and TCP	10 ppm	0.10 g /150 ml	0.125 kW, low pressure mercury vapor lamp	-	RhB = 97.58% (60) TCP: 92.99%	RhB: 0.184 TCP: 0.405	$^{\bullet}OH$	[158]
CuxZn(1x)O NPs/ H_2O_2	MB	10 μM	0.01 g	400W metal halide lamps	2.70	100% (120)	-	$^{\bullet}OH$	[159]
Ag_3VO_4/Cu-MOF/ rGO	AB 92	10 mg/L	10 mg/L	VL	-	95% (120)	0.008	$O_2^{\bullet-}$	[160]
$ZnFe_2O_4$@TiO_2/Cu	NPX	10 mg/L	5 mg/L	Sunlight	2.62	80.73% (120)	0.0166	$^{\bullet}OH$	[161]
CuO NPs	BV 3	100 mg/ L	0.05 g	Fluorescent lamp	-	86% (150)	0.0128	$^{\bullet}OH$	[162]
Cu_2MoS_4-Fe_3O_4@PPy-Ag	MG	10 mg/L	0.05 g	300 W XLS	-	94.8% (60)	0.0333	$O_2^{\bullet-}$ and $^{\bullet}OH$	[163]
FLN-Cu	MB	10 mg/L		UV		95% (60)	-	$^{\bullet}OH$	[105]
Cu-doped ZnO	MCP	-	0.5 g	-	2.88	90% (120)	-	$^{\bullet}OH$	[164]
$ZnO_{0.80}$–$CuO_{3.18}$/NCP $ZnS_{1.39}$–$CuS_{2.88}$/NCP	BP	30 mg/L	0.12 g/L	Medium-pressure mercury-vapor lamp (0.035 kW)	2.6 2.8	-	0.0012 0.0011	$^{\bullet}OH$, $O_2^{\bullet-}$ and h^+	[165]

Key: NPs: Nanoparticles; THL: Tungsten halogen lamp; XLS: Xenon light source; VL: Visible light; HPML: High pressure mercury lamp; U: Urea; CN: L-Asparagine; NC: Nanocomposite; [Cu(SCN)$_2$(phen)$_2$]: Diisothiocyanatobis (1,10-phenanthroline)copper(II) complex; CuO-CP: CuO supported Clinoptilolite; TNCuPc: Tetranitro copper phthalocyanine; Cu_2MoS_4-Fe_3O_4@PPy: Polypyrrole-functionalized Cu_2MoS_4 magnetic composites modified with Ag NPs; FLN-Cu: Fe_3O_4@LS@naphthalene-1,5-diamine@copper complex; FLN-Cu; MCP: monocrotophos pesticide; NCP: clinoptilo-lite NPs; BP: benzophenone; [C]: Pollutant concentration; [Cu]: Copper catalyst concentration; EoD: Degradation efficiency; Methyl blue: MB; BPA: bisphenol A; BB 41: Basic blue 41; AO 8: Acid orange 8; PAP: p-aminophenol; DR 16: Direct red 16; RG 19A: Reactive green 19A; O II: Orange II; AV 7: Acid violet 7; DB 71: Direct blue 71; FG: Fast green; p-ASA: p-arsanilic acid; AR 88; Acid red 88; AB 14: Acid brown 14; BV 3: Basic violet 3; PR: Phenol red; TC: Tetracycline; AR 1: Acid red 1; AB: Acid black; AO II: Acid orange II; TB: Toludine blue; MV: Methyl violet; TCP: Triclopyr; AB 92: Acid blue 92; MCP: Monocrotophos pesticide; NPX: Naproxen.

and time 15 mins) for the photocatalytic degradation of methyl orange (MO) in water medium ($E_g = 1.62$ eV). With a catalyst load of 30 mg, 20 mg/L of the MO was degraded under a VL by 91.4% in 100 mins, the mechanism of the degradation follows the equation (7-17).

$$Sm_2CuO_4 + h\nu(\text{visible}) \rightarrow Sm_2CuO_4\left(e^-_{CB}\right) + Sm_2CuO_4\left(h^+_{VB}\right) \quad (7)$$

$$Sm_2CuO_4(h^+) + H_2O \rightarrow H^+ + OH^{\bullet} + Sm_2CuO_4 \quad (8)$$

$$Sm_2CuO_4(h^+) + OH^- \rightarrow OH^{\bullet} + Sm_2CuO_4 \quad (9)$$

$$Sm_2CuO_4(e^-) + O_2 \rightarrow O_2^{\bullet-} + Sm_2CuO_4 \quad (10)$$

$$h^+ + O_2^{\bullet-} \rightarrow O_2 \quad (11)$$

$$2h^+ + 2H_2O \rightarrow 2H^+ + H_2O_2 \quad (12)$$

$$H_2O_{2(ads)} + e^- \rightarrow OH^{\bullet} + OH^- \quad (13)$$

$$O_2 + e^- \rightarrow O_2^{\bullet-} \quad (14)$$

$$O_{2(ads)} + e^- + H^+ \rightarrow {}^{\bullet}O_2H \quad (15)$$

$$O_2^{\bullet-} + OH^{\bullet} + H^+ \rightarrow H_2O_2 + O_2 \quad (16)$$

$$H_2O_{2(ads)} \rightarrow 2\ OH^{\bullet} \quad (17)$$

The utilization of ZnO semiconductor in the photocatalytic removal of organic contaminants has been immensely limited by its wide E_g (3.30 eV) [117]. The addition of perovskite-type metal oxides to ZnO showed enhanced photocatalytic property for the elimination of organic pollutants under VL. Therefore, Yulizar *et al.* [118] decorated ZnO with La_2CuO_4 and achieved improved photo-degradation of MG under VL. Within 120 mins, 91.0% degradation of the MG dye was achieved using VL irradiation. Similar reports involved the use of two phase $Lu_2Cu_2O_5/Lu_2O_3$ for the removal of thymol blue (TB), with 98.5% removal efficiency within 120 mins. Table 1 shows the extensive use of CBC as photocatalysts in the abatement of organic contaminants in water and the ROS involved in the development.

Another way of reducing the high possibility of charge recombination associated with the use of pure copper oxide semiconductor catalysts is the introduction of other semiconductors with suitable CB and VB to form heterostructures (*e.g.* Ag_3VO_4/TiO_2/graphene [166], CeO_2/TiO_2 [167], N,S-TiO_2/g-C_3N_4 [168]) with improved photocatalysis of organic pollutants. Luo *et al.* [147] prepared g-$C_3N_4/Cu_3B_2O_6$ hybrid photocatalysts using liquid chemisorption and thermal post-treatment technique and investigated the photocatalytic activity of the g-$C_3N_4/Cu_3B_2O_6$ as an oxidant under VL irradiation. The results demonstrated that the well-matched band edge structure between $Cu_3B_2O_6$ and g-C_3N_4 in the as-prepared g-$C_3N_4/Cu_3B_2O_6$ significantly supported separation and transfer of charge carriers when compared with individual $Cu_3B_2O_6$ and g-C_3N_4. The 60% g-$C_3N_4/Cu_3B_2O_6$ showed maximum k value of 0.0474 min^{-1}, which was 2.14 and 3.16 times higher than the $Cu_3B_2O_6$ and g-C_3N_4, respectively. The observed improvement in the photocatalytic performance was attributed to the boost in the separation efficiency of photogenerated e^--h^+ pairs with the combination of $Cu_3B_2O_6$ and g-C_3N_4, thus improving the activation of H_2O_2 for decolorization of MB under VL. After four cycles, the catalysts lost a slight degradation activity on the target pollutant. The degradation efficiency of Cu_2O and CuO-doped with Li_3BO_3 (Li_3BO_3/Cu_2O and Li_3BO_3/CuO, respectively) were investigated on the photocatalytic degradation of AV 7 by Ranjeh and co-workers [144]. Differences in the morphology and band gaps accounted for 5% difference in the photocatalytic degradation of the AV 7 by the two copper-oxide based catalysts. With lower crystalline size and E_g, the Li_3BO_3/Cu_2O demonstrated higher catalytic efficiency than the Li_3BO_3/CuO counterpart. Another

strategy is the use of plasmonic nano-metals to boost the photocatalytic property of copper oxides [124,169–171].

3.2. Fenton-like processes

Fenton reaction is renowned for its outstanding performance in the abatement of organic contaminants in water media [172–174]. In an ideal Fenton reaction, Fe(II) catalyses the decomposition of H_2O_2 to form $^{\bullet}OH$ (Eqs. (18–24)) [174]. The spontaneously generated $^{\bullet}OH$ destroys the structure of the pollutant due to its strong oxidation potential. More significantly, the generated Fe(III) can be reduced to Fe(II) through a similar reaction as represented in Eq. (2) [175], which guarantees steady generation of the $^{\bullet}OH$. In the case of an organic pollutant, the $^{\bullet}OH$ reacts with the organic compound to generate carbon-centred radicals. The $^{\bullet}OH$ although present in vanishing trace concentration reacts in well-defined ways with the organic pollutants, typically by abstraction of the H in O–H, N–H, or C–H bonds, in addition to the aromatic rings (Eqs. (25–27) [176,177]. Nevertheless, the use of the traditional Fenton reaction is commonly limited by its intrinsic limitations such as poor recyclability/reusability, accumulation of Fe-dense sludge, and slim working pH range. To circumvent these challenges, diverse heterogenous Fenton-like catalysts were devised as substitutes to the homogeneous processes [178–180].

$$Fe^{2+} + H_2O_2 \rightarrow Fe^{3+} + HO^- + OH^{\bullet} \quad (18)$$

$$Fe^{3+} + H_2O_2 \rightarrow Fe^{2+} + HO_2^{\bullet} + H^+ \quad (19)$$

$$OH^{\bullet} + H_2O_2 \rightarrow HO_2^{\bullet} + H_2O \quad (20)$$

$$OH^{\bullet} + Fe^{2+} \rightarrow Fe^{3+} + HO^- \quad (21)$$

$$Fe^{3+} + HO_2^{\bullet} \rightarrow Fe^{2+} + O_2H^+ \quad (22)$$

$$Fe^{2+} + HO_2^{\bullet} + H^+ \rightarrow Fe^{3+} + H_2O_2 \quad (23)$$

$$HO_2^{\bullet} + HO_2^{\bullet} \rightarrow H_2O_2 + O_2 \quad (24)$$

$$OH^{\bullet} + R{-}H \rightarrow H_2O + R^{\bullet} \quad (25)$$

$$OH^{\bullet} + C{=}C \rightarrow HO{-}C{-}C^{\bullet} \quad (26)$$

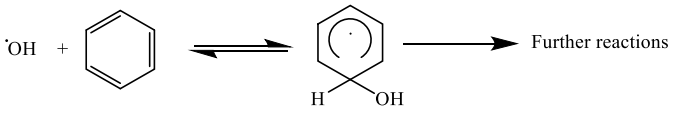

(27)

Nowadays, Cu-based materials have been widely used as catalysts in Fenton-like reactions for the effective elimination of organic contaminants in water, owing to their outstanding characteristics such as eco-friendliness, cost-effectiveness, high stability, high natural abundance and efficient catalytic activity [181]. Table 2 summarises the reaction conditions and performance of Cu-based catalysts in Fenton-like reactions towards the removal of organic contaminants in water. In addition, owing to its broad range of existence in various oxidation states (Cu^0, Cu^+, Cu^{2+}, and Cu^{3+}), CBC can participate and promote Fenton-like reactions [182]. The rate of reduction of Cu^{2+} by H_2O_2 is fast (4.6×10^2 $M^{-1}s^{-1}$) and Cu^+ can efficiently react with H_2O_2 to generate $^{\bullet}OH$ radical with a high reaction rate (1×10^4 $M^{-1}s^{-1}$) [183]. Contemporary research has revealed that organic contaminants can form bonds with Cu catalysts species, generating orbital interactions that involve the mobility of electrons in the form of $\pi\rightarrow Cu^{2+}$. This process leads to the decrease of high oxidation state Cu and accelerates the decomposition of H_2O_2 into more $^{\bullet}OH$ [184,185]. Moreso, in Fenton-like reactions, electron distribution tuning has been shown to be an effective strategy for enhancing catalytic performance [186]. The negative and the positive areas in the distribution of electrostatic potential are anticipated to be favourable reactive sites for redox reactions of H_2O_2 [187]. Lyu *et al.* applied phenoxyphenol functionalized reduced graphene oxide nanosheets (POP-rGO NSs) in Fenton-like process catalysis and realized that the surface complexation of POP with rGO via C–O–C bridges enhanced the uneven dispersal of electrons in the catalyst, resulting in efficient H_2O_2 decomposition on the electron-poor and electron-rich centres around the C and O atoms, respectively [188]. Furthermore, the charge redistribution in some materials polarized the related orbits and atoms to generate an internal electric field (IEF) [189]. Effects such as promotion of charge transfer, reduction of diffusion and improvement of accessibility of charge to reactants are reported to be driven by the IEF [190]. These effects are also reported for semiconductor catalysts like copper oxides [191–193]. For example, Li *et al.* [193] prepared a framework of Cu-doped boron nitride nanobelts (Cu-BN, Fig. 6) with an IEF arising from the uneven dispersion of electrons with electropositive Cu sites and electronegative N sites. This was used for the oxidative decomposition of BPA in a Fenton-like process. The unique architecture enhanced the oxidation of H_2O on the electropositive Cu sites and the reduction of H_2O_2 molecules on the electronegative N sites, generating highly reactive $^{\bullet}OH$. This acceleration facilitated the abatement of BPA adsorbed on Cu-BN system. Typically, the electron paramagnetic resonance (EPR) results confirmed that BPA donated electrons to Cu through the $\pi\rightarrow Cu^{2+}$ interaction in the σ–Cu–ligand complexes between the Cu surface and phenolic groups, followed by the oxidation of the pollutant.

Gong *et al.* [194] utilized artificially designed Cu-Schiff bases nanozyme (Cu@SB) to realize efficient activation of H_2O_2 for the degradation of amlodipine (AD), achieving 100% degradation within 90 mins at a temperature of 45 °C. Schiff bases were used as special donor ligands that efficiently stabilized the active copper ion. The removal complied with a pseudo first-order kinetic model, while $^{\bullet}OH$ and singlet oxygen ($^1O_2$) were the key reactive species in the degradation process. The Fenton-like activity was driven by the redox reactions between Cu^+/Cu^{2+}. The *k* value of the AD degradation increased with increasing catalyst, H_2O_2 concentrations, pH, and temperature. Naz and team [197], also prepared and analyzed a silica-based Cu^{2+} organic-inorganic hybrid compound, achieved by grafting of Schiff base onto silica surface and complexation of the base by $CuCl_2$. The as-prepared metal complex hybrid heterogeneous catalyst was effective in the oxidative degradation of a non-biodegradable RB5 azo dye in the presence of H_2O_2 to generate $^{\bullet}OH$ free radicals. At the best reaction parameters for optimal degradation of RB5, 91% of the recalcitrant dye was removed in 100 mins, at a *k* degradation rate of 0.017 min^{-1}. The possible mechanism indicates that the molecules of H_2O_2 were activated first by the Cu^{2+} hybrid catalyst to form the $^{\bullet}OH$ radical. The generated $^{\bullet}OH$ radical attacks the organic substrate, bringing about the chemical decomposition of the substrates through abstraction of H and addition to the C=C bonds [206]. Therefore, the generated $^{\bullet}OH$ radicals reacts with the RB5 and is transformed to dye-radical products as shown in Eq. 28:

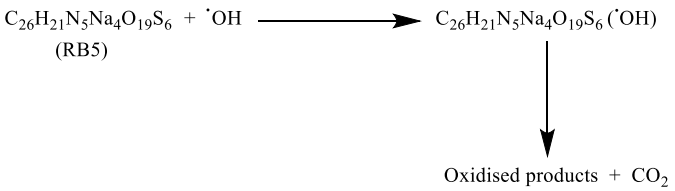

(28)

2

Ma and co-workers [181] incorporated Cu^{+} into g-C_3N_4 towards the removal of various contaminants. When g-C_3N_4 is generated, the Cu^{2+} is reduced to Cu^{+} by the release of nitride and carbon fragments, thereby fostering Fenton-like activation of H_2O_2. The removal efficiencies of 84.4%, 94.6%, 96.0% and 99.2% were recorded for TC, BPA, AR 73 and RhB, respectively, positing that the Cu(I)-doped g-C_3N_4 (Cu(I)-g-C_3N_4) was an efficient Fenton-like catalyst to remove various organic pollutants. Interestingly, the narrow pH window associated with the Fenton process was overcome by this Fenton-like process as the degradation of RhB enjoyed a broad pH window of 3-11. Increasing the Cu metal load on the g-C_3N_4 was reported by Zhu *et al.* [61] to increase the amount of Cu-N_x species which accelerated the H_2O_2 decomposition to generate $^{\bullet}OH$. Consequently, the Cu-g-C_3N_4 demonstrated superior catalytic properties for the removal of MB, MO, and RhB (Table 1). Copper-iron based bimetallic systems have demonstrated a broad range of heterogeneous catalysis including oxidation of phenol [207] and toluene [208], and heterogeneous Fenton degradation of phenolics [209,210], RhB [211], DPD [203], SA [202], and SMX [200]. Fig. 7A portrays a probable mechanism of reaction of SMX degradation using $Fe_{0.75}Cu_{0.25}$ (BDC).

In a report by Gao *et al.* [198], the efficiency of a coupled Fenton-like and photocatalytic process using Cu_2O/BiOBr with S-scheme heterojunction in the decomposition of organic solvents such as CR, MB, MV, RhB, TC, and a mixture of the contaminants was described. The reduction of glucose remarkably restored the photocatalysis of the Cu_2O/-BiOBr catalyst to ≈90% from ≈60% (after 4 cycles). Here, a Fenton-like Cu_2O and stable BiOBr were employed to generate the IEF (Fig. 7B), which functioned as the driving potential for the migration of photo-induced charge. This configuration supported the separation of

Table 2
Reaction conditions and performance of Cu-based catalysts in Fenton-like reactions towards the removal of organic contaminants in water

Reaction conditions						Efficiency of catalyst				
Catalyst	Contaminant	[C]	[Cu]	[H_2O_2]	pH	[EoD](min)	k_{abs} (min^{-1})	[TOC] (min)	KRS	Reference
Cu@SB	AD	10 μM	10 -50 ppm	0.5 mM -2.0 mM	5-9.0	100% (90)	0.0168 @ 35 °C		$^{\bullet}OH$ and $O_2^{\bullet-}$	[194]
Cu-doped MgO	SA	50 ppm	500 ppm	20 mM	10.8–11	100% (45)	0.042	100% (45)	$^{\bullet}OH$ or $^{\bullet}HO_2/O_2^{\bullet-}$	[62]
Cu(I)-g-C_3N_4	RhB	50 ppm	80 ppm	40 mM	7	99.2% (60)	-	22.8% (60)	$^{\bullet}OH$, and $O_2^{\bullet-}$	[181]
Cu-g-C_3N_4	RhB	10 ppm	20 ppm	300 mM	7	92.3% (15)	-	42% (60)	$^1O_2$, $O_2^{\bullet-}$, and $^{\bullet}OH$	[61]
Cu-doped Fe@Fe_2O_3/CNT/Ni	TC	20 ppm	-	-	3	98.1% (120)		89.8% (6 h)	$^{\bullet}OH$	[195]
Cu−Zn−Fe-LDH	ACT	0.1 mmol/L	0.5 g/L	30 mmol/L	7	100% (24h)	-	-	$^{\bullet}OH$	[196]
Cu (II)-hybrid	RB 5	45 ppm	17.6 mM	0.8 g/L		91% (100)	0.017		$^{\bullet}OH$	[197]
Cu_2O/BiOBr S-scheme	MB, RhB, CR, MV, TC	100 ppm	50 mg	0.5 mL	4–10	MB: 98% (50) RhB: 82% (50) CR: 95% (50) MV:86% (50) TC:100% (50)	0.0787 @MB		$^{\bullet}OH$	[198]
$Ni_{(2-x)}Cu_{(x)}$Al-LDH	SPRW	80 ppm	0.4 g/L	-	5	100% (90)	0.0316	74.8% (90)	$^{\bullet}OH$	[199]
$Fe_{0.75}Cu_{0.25}$ (BDC)	SMX	20 ppm	6 mM	0.5 g/L	4.0-8.6	100% (120)	-	-	$^{\bullet}OH$	[200]
5Fe2.5Cu-Al_2O_3	NB	100 ppm	0.5 g/L	300 μL	3.0	100% (60)	-	-	$^{\bullet}OH$	[201]
Cu-BN(2.84 wt% Cu)	BPA	25 ppm	1.0 g/L	5 mM	3–11	100% (30)	0.198	64.2% (120)	$^{\bullet}OH$	[141]
Fe/Cu/Al-pillared clays	SA	0.29 mmol/L	2.0 g/L	5.23 mmol/L	3.5	98% (240)	-	-	$^{\bullet}OH$	[202]
CuFe/SBA-15 bimetallic	DPD	0.1 g/L	0.1 g/L	8 mM	4	90% (120)	-	70% (120)	$^{\bullet}OH$	[203]
$Cu^{2+}/H_2O_2/Cl^{-}$	CMZ		1 μM	10 mM	7	96% (120)	0.028	-	$^{\bullet}OH$, and $O_2^{\bullet-}$	[204]
CuO NPs/H_2O_2	Alachlor Ph	30 ppm 0.5 ppm	0.2 g 0.1 g	2 mL	4-9	100% (30)	0.292	- -	$^{\bullet}OH$, or $^{\bullet}HO_2^{-}$	[205]

Key: LDH: Layered double hydroxide; Cu (II)-hybrid: SiO_2*NH_2*QC*Cu; QC: 2-Quinolinecarboxaldehyde; x = 0.0; 0.5; 1.5; and 2.0; SPRW: synthetic petroleum wastewater; $Fe_{0.75}Cu_{0.25}$ (BDC): Iron and copper bimetallic MOF material; Cu-doped boron nitride nanobelts; DPD: N, N-diethyl-p-phenyl diamine; SA: Sulfanilamide; CMZ: Carbamazepine; SMX: Sulfamethoxazole; Ph: Phenanthrene; AD: Amlodipine; RB 5: Reactive black 5; NB: Nitrobenzene.

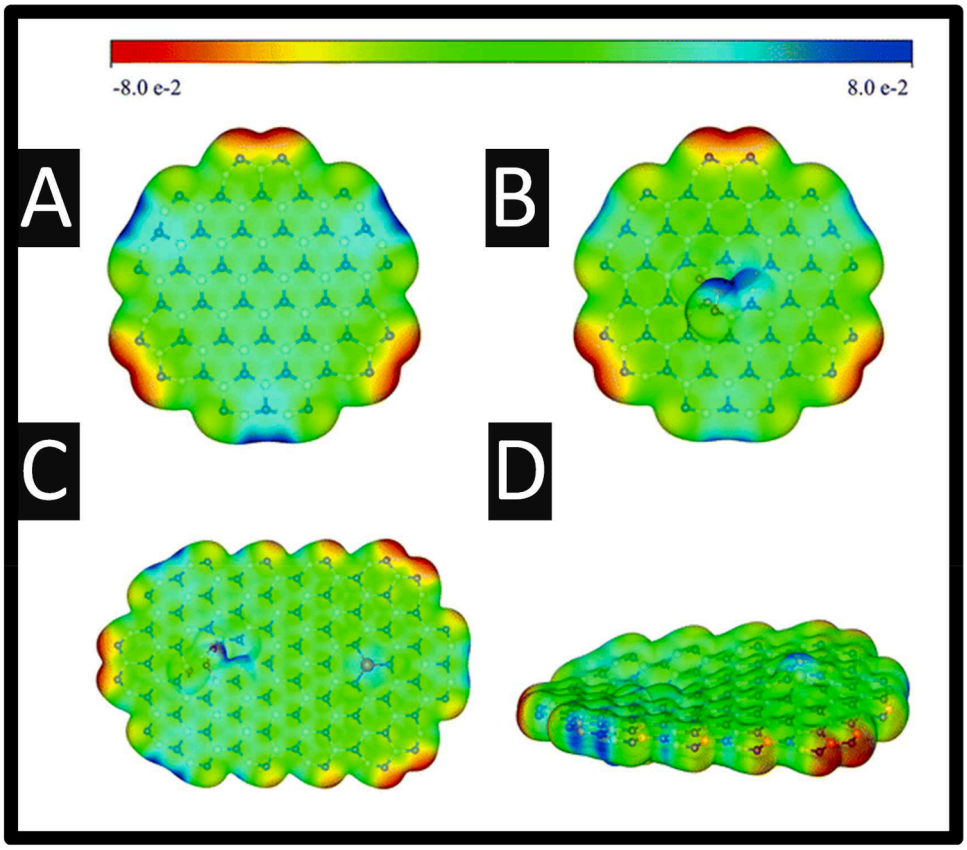

Fig. 6. A framework of Cu-doped boron nitride nanobelts (Cu-BN) showing ESP distribution for (A) perfect BN, (B) the as-prepared BN , (C) the plan map of ESP and (D) 3D-map for Cu-doped BN. (orange, red, pink, blue, and white circles represent Cu, O, B, N, and H atoms respectively). Reproduced from reference [193]. Copyright 2019 The Royal Society of Chemistry.

photoinduced carriers and generation of the $^{\bullet}OH$ by H_2O_2 and Cu^+, leading to successful photocatalytic decomposition of organic contaminants. Interestingly, during irradiation by light, the prevalence of the in-built electric field can result in the photoinduced e^- in the BiOBr CB combining with the h^+ in the Cu_2O VB. Simultaneously, the h^+ in the BiOBr VB and the e^- of the Cu_2O CB are preserved for photo-redox reactions (Fig. 7C). This path of charge transfer demonstrates that the prepared heterojunction between Cu_2O and BiOBr is S-scheme heterojunction. This heterojunction promoted the aggressive oxidation and reduction qualities of the 15%Cu_2O/BiOBr, thereby promoting the efficient degradation of pollutants through coupled Fenton-like and photocatalytic processes.

3.3. Persulfates activation

The AOPs based on PS such as peroxydisulfate (PDS, $S_2O_8^{2-}$) or peroxymonosulfate (PMS, HSO_5^-) as efficient and auspicious methods for the abatement of organic pollutants in water have attracted a growing popularity in the last decade [18,212,213]. The activation of PMS or PDS generates powerful single-electron $SO_4^{\bullet -}$ [214,215] with advantages of higher redox potentials (2500-3000 mV) than that of $^{\bullet}OH$ (1800–2700 mV) [216], long half-life (0.03–0.04 ms) [217], and high selectivity [218]. In addition, $SO_4^{\bullet -}$ radicals can efficiently react with target contaminants over a wider window of pH values (2–8) [219,220]. The sulfate radicals can decompose recalcitrant organic pollutants in water and generate inorganic salt, H_2O, CO_2, and other lower molecular substances [221,222]. Many scientific reports have demonstrated that PS-based AOPs can effectively degrade refractory contaminants including PPCPs, antibiotics, dyes, chlorinated organic contaminants, phenolics, and endocrine-disrupting chemicals (EDCs) [216,223–227]. The PMS and PDS are typified by the presence of O–O bonds [215], and O–O bonds can generate reactive radicals that degrade pollutants [228]. Relative to other oxidants, such as O_3 and H_2O_2, the PS are more convenient to transport and store because of their existence as solid powder.

Nonetheless, the direct activation of the PMS and PDS to generate the sulfate radicals for the abatement of most organic contaminants are terribly slow, which demands additional physical or chemical stimulation for practical application. In a review by Tian *et al.* [216], the activation of the PMS and PDS to generate reactive radicals were achieved with various strategies such as conventional (thermal, alkaline, UV, and transition metal ions activations), and modern (microwave, metal oxide, and carbon activation). Among these strategies, the interest in the use of heterogenous catalysts have peaked because of their high catalytic activity, exceptional reusability, and less energy requirement [39,229]. Hence, huge attention has been given to investigating heterogeneous catalysts for PS activation and CBC have enjoyed such attention for their effectiveness in the abatement of organic contaminants in water. Table 3 presents an overview of the reaction conditions and performance of PMS-based catalysts in the abatement of organic contaminants. For instance, Wang *et al.* [230] showed that adding Cu^{2+} not only enhanced the effectiveness of degradation of Fe^{2+}/hydroxylamine (HA)/PS platforms, but also widened the pH window of Fe^{2+}/HA/PS decomposition of O II (pH; 2–10). Scavenger reactions reveal that $SO_4^{\bullet -}$ is the main ROS. The degradation followed different pathways in the acidic and basic medium, both favourable by the introduction of the Cu^{2+} ion. In the acidic range, Cu^+ was oxidized to Cu^{2+} by Fe^{2+}, while in the basic environment, HA reduced Cu^{2+} to Cu^+ to produce the $SO_4^{\bullet -}$ (Eqs. 29–30) by activating PS, which extended the pH to the alkaline range in the use of the Fe^{2+}/HA/PS for the elimination of O II.

$$NH_2OH + Cu^{2+} \rightarrow Cu^+ + \text{Nitrogenous products} + H^+ \quad (29)$$

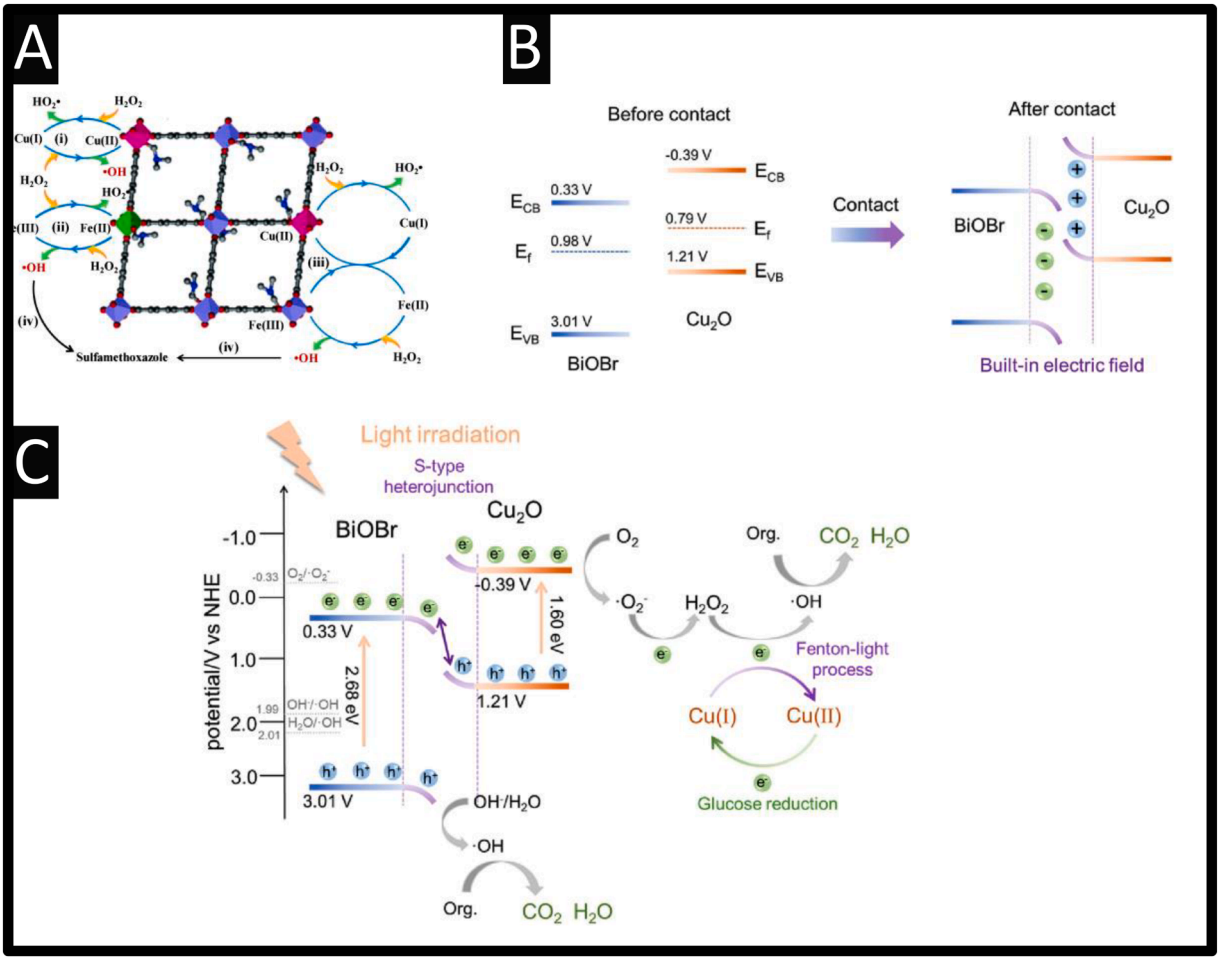

Fig. 7. **A:** Probable mechanism of reaction of SMX degradation using $Fe_{0.75}Cu_{0.25}$ (BDC). Figure reproduced from reference [200]. Copyright 2020 Elsevier. **B:** The band structure of Cu_2O and BiOBr; **C:** Schematic diagram of synergism between Fenton-like process and S-scheme heterojunction. Figure reproduced from reference [198]. Copyright 2023 Elsevier.

$$Cu^{+} + S_2O_8^{2-} \rightarrow Cu^{2+} + SO_4^{-} \quad (30)$$

3.3.1. *Peroxymonosulfate (PMS)*

Lei and co-workers [238] revealed that copper ferrite-graphite oxide hybrid ($CuFe_2O_4$@GO) catalyst could activate PMS for the abatement of MB in solution. A removal efficiency of 93.3% was realized when 0.8 mmol/L PMS and 200 ppm $CuFe_2O_4$@GO were applied on 20 ppm of MB at room temperature condition. The $CuFe_2O_4$@GO catalyst presented outstanding stability and reusability. Additional investigation on the mechanism of oxidation of MB showed that the Cu^{2+}/Cu^{+} redox couple on $CuFe_2O_4$@GO performed the key role in the activation of PMS, where both sulfate and hydroxyl radicals were produced and led to the decomposition of the targeted contaminants. Although the use of Cu^{2+}/Cu^{+} redox cycles have been very significant in the activation of PMS in the Fenton-like processes, the conversion of Cu^{2+} to Cu^{+} is characteristically very slow [262], especially in acidic or neutral conditions [263]. Huang *et al.* [257] demonstrated that the addition of Cl^{-} makes it possible for the Cu^{2+}/PMS system to oxidize acid orange (AO7) in neutral, acidic, and alkaline solution (pH range of 4-9). This result demonstrates the significance of Cl^{-} concentration in accelerating the efficiency of oxidation of the Cu^{2+}/PMS system under different pH values, which is hardly employed in the trace Cu(II) supported PMS system in saline wastewater. The degradation of AO7 followed a pseudo first-order with k that was linearly correlated with increasing Cl^{-} concentration (0–300 mM). The AO7 was completely abated in the presence of 100 mM of Cl^{-} in 60 mins. The scavenger experiments and EPR measurements showed that $^1O_2$ was the ROS in the Cu^{2+}/PMS system. Nonetheless, some undesirable by-products were identified in the degradation pathway of the AO7, thus signalling a need to be cautious in the evaluation of the use of Cu^{2+}/PMS system in chloride-containing solutions.

Yang *et al.* [240] synthesized diverse crystalline MnO_2 (C-MnO_2) and single and bimetallic-doped amorphous MnO_2 described as M-AMO, where M represents Cu, Co, Fe and Ni for organic oxidation with PMS. The result showed that at a concentration of 1 mol%, the M-AMO demonstrated higher catalytic activities than C-MnO_2, while the Cu-AMO catalysed PMS system presented k value that is at 3.5 times more than that of Co-AMO, Fe-AMO, and Ni-AMO. The non-radical degradation of target pollutant phenol followed two pathways (Fig. 8). The first pathway (pathway 1) is the overall PMS activation mechanism through a direct transfer-electron process (DTP) and the second pathway (pathway 2) is the oxidation of phenol. In pathway 1 detailing the DTP mechanism for both AMO/PMS and Cu-AMO/PMS platforms, the PMS bonds firstly with the surface of the catalysts to generate an aggressive $Mn^{3+}_{(s)}$–(HO)OSO_3^{-} intermediate, attacking phenol through inner-sphere interactions with the transfer of one-electron over the AMO/PMS and Cu-AMO/PMS surface. With the generation of $Mn^{3+}_{(s)}$–(HO)OSO_3^{-} intermediate, $Mn^{3+}_{(s)}$ is oxidized to $Mn^{4+}_{(s)}$, meanwhile transferring the lost one-electron to HSO_5^{-}. Phenol is consequently oxidized by losing one electron to the activated PMS. As a result, the surface adsorbed PMS gains two electrons from phenol and $Mn^{3+}_{(s)}$ and decomposes to OH^{-} and to SO_4^{2-}, resulting in the simultaneous oxidation of phenol and $Mn^{3+}_{(s)}$.

Table 3
Reaction conditions and performance of PMS-based catalysts in the abatement of organic contaminants

Reaction conditions						Efficiency of catalyst				
Catalyst system	Contaminant	[C]	[Cu]	[PMS]	pH	[EoD](min)	k_{abs} (min^{-1})	TOC(min)	KRS	Reference
Fe(III)/ Cu^{2+}/HA/PMS	AO7	-	1 μM	1 mM	3-10	100% (5)	0.569	-	$^{\bullet}OH$, and $SO_4^{\bullet-}$	[231]
CT/HA/PS	AO7	0.06 mM	0.1 g/L	0.5 mM	3-5	99.69% (20)	0.128 @ 0.5 mM HA	68.26%	$SO_4^{\bullet-}$	[232]
Cu-doped (110)/PMS/ Light	BPA	50 mg/L	10 mg	15	3–9	84.79%	0.059	95%	$^1O_2$ and $O_2^{\bullet-}$	[233]
HA/Cu^{2+}/PMS	RhB	10 μM	50 μM	0.4 mM	5.0	91.1% (30)	-	-	$^{\bullet}OH$ and $SO_4^{\bullet-}$	[234]
CuOx/OMS-2	RhB	2.5×10^{-4}	5 mg	0.83 mmol/L	-	98% (3.73)				[235]
Cu (II)/PMS	2,4-DCP; BTA; 1,4-D; and toluene	10 μM	10 μM	400 μM	8	2,4-DCP = 93% BTA = 88% 1,4-D = 79% Toluene = 68%	0.1707 for 2,4-DCP	-	Cu (III) and $^{\bullet}OH$	[236]
PMS/CuO	BPA	5 mg/L	10	1.0 mM	3.2–9.4	100% (60)	0.0979	50%	$^1O_2$	[237]
$CuFe_2O_4$@GO	MB, RRD, AO7 and RhB	20 mg/L	200 mg/L	0.8 mmol/L	11	93.3% (30) for MB	-	-	$SO_4^{\bullet-}$and $\bullet OH$	[238]
Cu_3P	SMX	0.5–4.1 mg/L	20–80 mg/L	0.05–1 g/L		100% (20)	0.200		$SO_4^{\bullet-}$	[239]
Cu-AMO–PMS complex-based	Phenol	0.22 mM	0.1 g/L	0.65 mM	3.0 to 8.0	100% (60)	0.087	-	$SO_4^{\bullet-}$ and $^{\bullet}OH$	[240]
$CuFe_2O_4$/PMS	p-ASA	10 ppm	0.2 g/L	1 mM	4.26	85% (60)	0.0311		$SO_4^{\bullet-}$, $^{\bullet}OH$ and $O_2^{\bullet-}$	[241]
CuS/PS	ATZ	25 mmol/L	35 mmol/L	4 mmol/L	2.5	91.5% (40)	0.808	-	$^{\bullet}OH$ and $SO_4^{\bullet-}$	[242]
CuO/Fe_2O_3/$CuFe_2O_4$	LEF	10 ppm	50 mg	1.5 g/L	4.33 to 9.37	75.5% (120)	-	64.5% (120)	$SO_4^{\bullet-}$, $^{\bullet}OH$ and $O_2^{\bullet-}$	[243]
Boric acid/Cu/PMS	RhB	10 ppm	10 μM	0.4 mM	10	100% (5)	-	-	$SO_4^{\bullet-}$ and Cu(III)	[244]
CuOx@Co-LDH	Phenol	0.1 mM	0.3 g/L	S4 mM	5.0–12.0	100% (40)	0.170	-	$SO_4^{\bullet-}$, $^{\bullet}OH$ and $O_2^{\bullet-}$	[245]
Cu@C/SiO2 NFMs	TCH	10 ppm	0.3 g/L	5 mg/L	4-10	95% (40)	0.054	-	$^{\bullet}OH$ and $SO_4^{\bullet-}$	[246]
Cu^{2+}/Fe(VI)	SMX	5 μM	20 μM	-	7.0	100% (8)	2.41	-	$O_2^{\bullet-}$	[247]
CoOOH-Cu/PMS	TC	22.5 μM	0.2 g/L	0.2 mM	7.0	97.7% (10)	0.6482	60.7% (60)	$O_2^{\bullet-}$	[248]
MS-(AgC)/Cu	HEPES	50-200 ppm	1-2 g/L	0.5-2 g/L	7.10	98.3% (30)	0.1138	61.60% (30)	$SO_4^{\bullet-}$ and $^{\bullet}OH$	[249]
Cu^+/g-C_3N_4(1:4)/ Sunlight	RhB	10 mmol/L	0.5 g/L	0.5 mmol/L	2.0–10.0.	95.7% (30)	-	-	$SO_4^{\bullet-}$, $^{\bullet}OH$, h^+ VB, $^1O_2$, and $O_2^{\bullet-}$	[250]
NBC-Fe-Cu	SMX	15 ppm	0.05 g/L	1.2 mM	7	91.6% (60)	0.0403	-	$^{\bullet}OH$, $O_2^{\bullet-}$ and $^1O_2$	[251]
UV–vis light/ $Zn_{0.8}Cu_{0.2}Fe_2O_4$/ sulfite	ATZ	4.4 μM	200 ppm	0.5 mM	7.2	95% (30)	0.2	-	$SO_4^{\bullet-}$	[252]
40%-$CuFe_2O_4$ NPS/ kaolinite	BPA	50 ppm	0.5 g/L	0.5 mM	7.0		0.0589	55% (60)	$SO_4^{\bullet-}$	[253]
Fe-Cu@N-C	O II	20 ppm	0.04 g/L	20 mg	-	100% (50)	-	~66.1% (50)	$^1O_2$	[254]
CuHNPs-7.5/VL/PMS	TC	40 ppm	0.20 g/L	0.45 mM	2.14 to 10.75	97.80% (30)	0.1254		$SO_4^{\bullet-}$, $^{\bullet}OH$ $O_2^{\bullet-}$ and $^1O_2$	[255]
ZCFO/PM	CIP	10 ppm	10 mg	2.5 mM	7.5	96.6% (15)	1.90	70% (60)	$SO_4^{\bullet-}$, $^{\bullet}OH$ $O_2^{\bullet-}$ and $^1O_2$	[256]
Cu^{2+}/PMS	AO7	0.05 mM	0.08 mM	3 mM	9.0	98.6% (60)	0.0475	46% (60)	$^1O_2$	[257]
Cu-TCPP(BA)-MOF/VL	RhB	10 ppm	0.1 g/L	0.1 g/L	7	100% (40)	0.9011	-	$^1O_2$	[67]
Zero valent copper	2,4-DCP	5 ppm	1 mM	0.5 mM	3.1	100% (10)	0.557	56.7% (120)	$SO_4^{\bullet-}$ and $^{\bullet}OH$	[258]
Nano zero valent copper						100% (10)	1.122	45.3% (120)		
Cu/PTI(C6N8.7Cu)/ VL	RhB	10 ppm	0.1 g	0.1 nM	3–10	96.2% (60)	-		$O_2^{\bullet-}$, $^1O_2$, h^+ VB, and $SO_4^{\bullet-}$	[259]
Cu-NC/PMS (1.85 wt% Cu)/H_2O_2	TC	20 ppm	0.2 g/L	1 mM	5.0	91.3% (40)	0.0762	-	$^{\bullet}OH$	[260]
AM/PM	RhB	20 ppm	0.3 g/ L	0.5 mM	3–10	100% (13)	0.34761	-	$SO_4^{\bullet-}$ and $^1O_2$	[261]

Key: CT/HA/PS: Copper tailings/hydroxylamine/persulfate; OMS-2: α-MnO_2 octahedral molecular sieves; BTA: Benzotriazole; 2,4-DCP: 2,4-dichlorophenol; MS-(AgC)/Cu: Magnetic-chitosan/amine supported CuNP; NBC: Natural biochar; Fe-Cu@N-C: Fe, Cu-coordinated ZIF-derived bimetal encapsulated N-doped carbon nanotubes; CuHNPs-7.5: Cu-doped hematite nanoplates; ZCFO: copper substituted zinc ferrite; Cu/PTI: poly(triazine imide) (PTI) with intercalation of Cu ion heterogeneous catalysts; Cu-NC/PMS: copper supported polyurethane foam; AM: recycled anode material; 2,4-DCP: 2,4-dichlorophenol; 1,4-D: 1,4-dioxane; LEV: Levofloxacin; HEPES: [4-(2-hydroxyethyl)-1-piperazineethanesulfonic acid]; CIP: Ciprofloxacin; TCH: Tetracycline hydrochloride; RRD: reactive X-3B red dye.

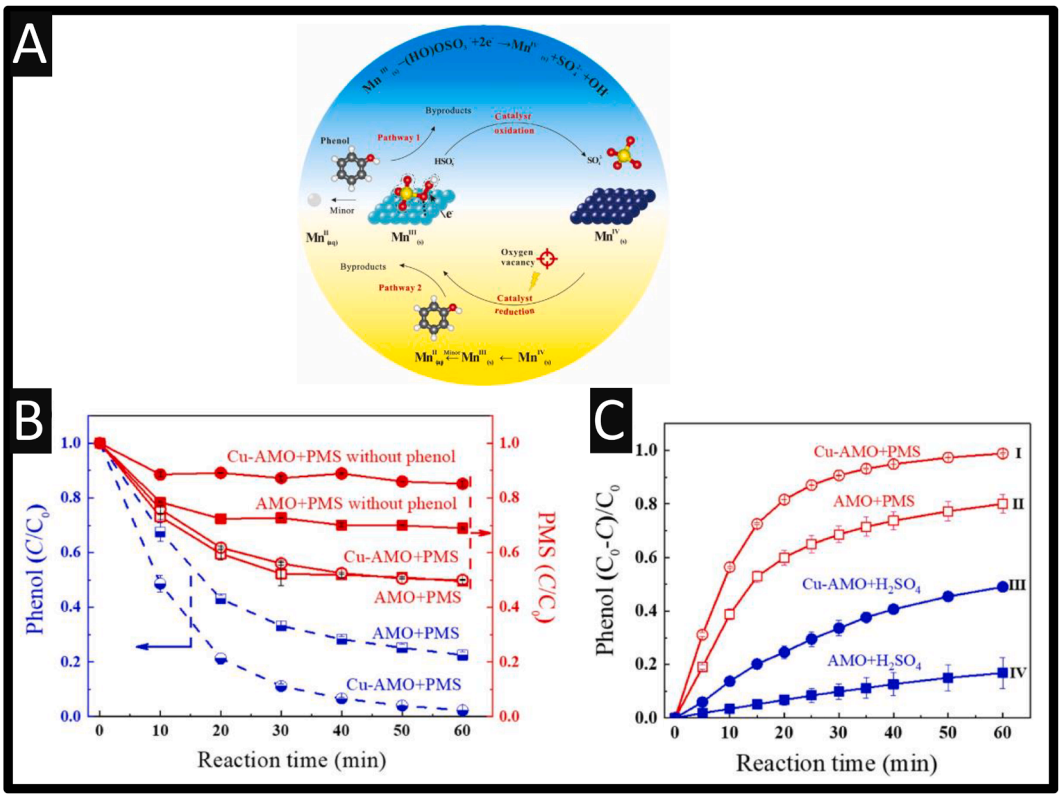

Fig. 8. **A:** The schematic representation of non-radical degradation of Phenol following two pathways; **B:** Phenol degradation and PMS consumption using AMO and Cu-AMO; **C:** catalytic degradation of + PMS or H_2SO_4. Conditions of experiment: $[catalysts]_0$ 100 ppm $[PMS]_0$ 0.65 mM, $[phenol]_0$ 0.22 mM, pH_0 3.2 and T 30°C. Figure reproduced with permission from reference [240]. Copyright 2021 Elsevier.

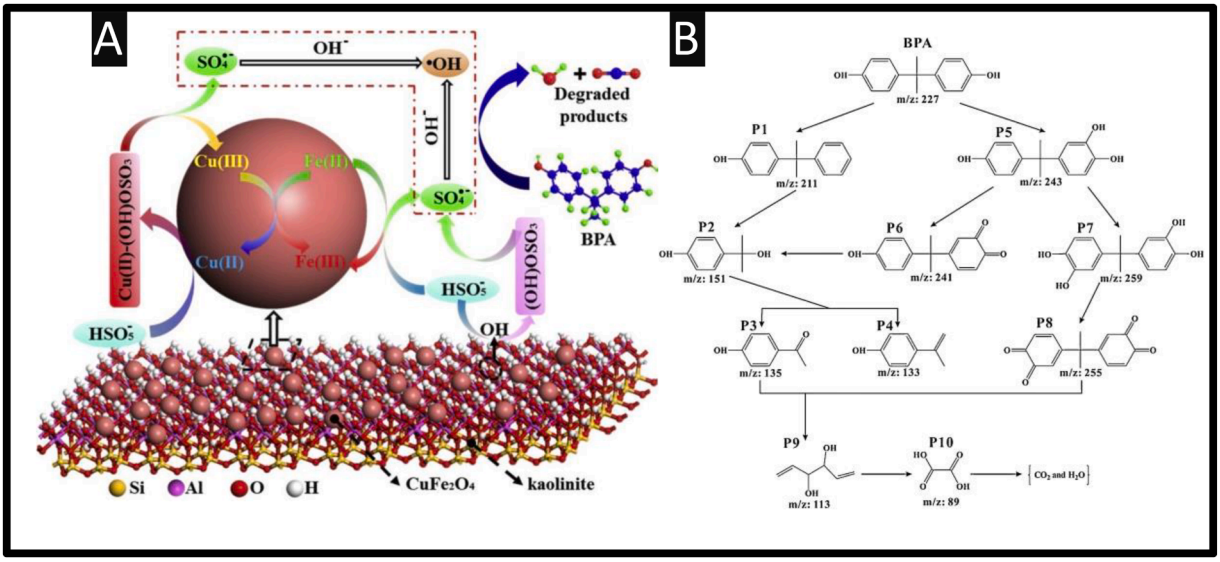

Fig. 9. **A:** The reaction mechanism for the decomposition of BPA in the $CuFe_2O_4$/kaolinite system; **B:** The probable mechanism for the decomposition of BPA. Figure reproduced from reference [253]. Copyright 2019 Elsevier.

Fig. 8A shows a schematic representation of non-radical degradation of phenol following two pathways and Fig. 8B shows phenol degradation and PMS consumption using Cu-AMO and AMO. The superior performance of Cu-doped AMO in the Cu-AMO/PMS system was attributed to the generation of copious high-valence Mn species, which invariably strengthened direct oxidation process (DOP) mechanism. In addition, doping with Cu had a significant effect on the charge transfer and surface electron through generation of more O_2 species. The lattice distortion caused by the Cu dopant allowed more K^+, resulting in the increase of the Mn^{4+}/Mn^{3+} ratio of the Cu-AMO lattice, which improved DOPs for direct oxidation of phenol by the rich-valence Mn^{4+}. Doping with Cu resulted in less leaching of $Mn^{2+}_{(aq)}$, a better crystallinity of AMO, and higher O_2 vacancies, driving the redox circling between $Mn^{4+}_{(s)}$ and $Mn^{3+}_{(s)}$ in the DTP and DOP mechanisms. Hence, the greater presence of $Mn^{4+}_{(s)}$ in Cu-AMO supported the DOPs; in the interim, the generated $Mn^{3+}_{(s)}$ aids coordination with PMS for the formation of the reactive

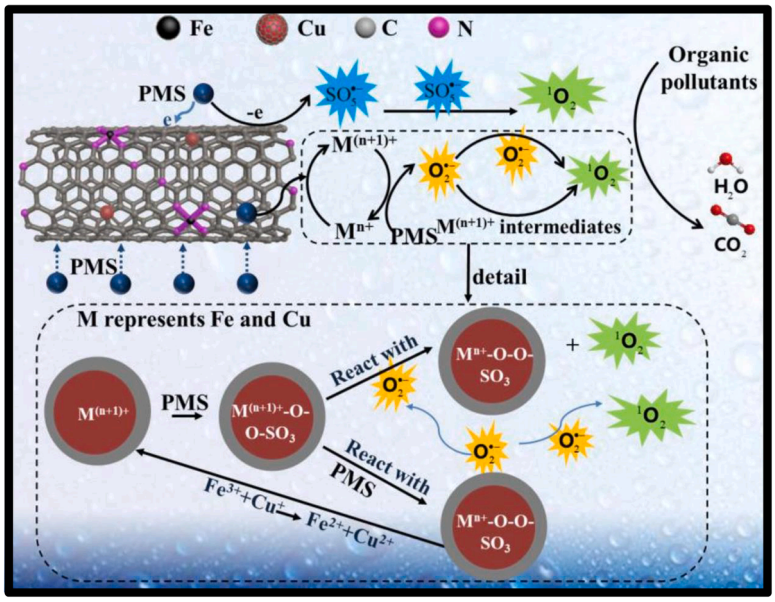

Fig. 10. Suggested non-radical mechanism of reaction using the Fe-Cu@N-C-950/PMS system. Figure reproduced from reference [254]. Copyright 2021 Elsevier.

complex towards the abatement of phenol through the DTP route. In addition, the possibility of copper leaching will be insignificant to the activation of PMS and decomposition of phenol.

Dong and co-workers [253] reported the preparation of $CuFe_2O_4$/-kaolinite catalysts via a simple citrate combustion technique. The prepared catalysts were assessed for their capacity to activate PMS towards the oxidative degradation of BPA. Higher SSA, more OH groups, larger pore volume, and more available reactive sites were realized at 40%-$CuFe_2O_4$ NPs/kaolinite catalyst ratio, which resulted in effective activation of the PMS. As seen in Fig. 9A, monodispersed $CuFe_2O_4$ NPs were evenly hinged on the Fe–O–Al bond, which hinders metal ions leaching and supported exceptional reusability. The degradation of BPA also followed two pathways (Fig. 9B), including the generation and decomposition of $\equiv Cu^{2+}$-(HO)OSO_3−(Cu^{2+}/Cu^{3+} and Cu^{3+}/Cu^{2+} redox reaction) and the oxidation of $\equiv Fe^{2+}$.

Yao *et al.* [254] proposed a new Fe, Cu-coordinated ZIF-based bimetal encapsulated N-doped CNT (Fe-Cu@N-CNT). This material boasts abundant bimetallic active sites (Fe-Nx and Cu-Nx), a large surface area, high levels of N-doping and a conducted porous carbon structure, facilitating rapid electron and mass transport. These attributes collectively contributed to the outstanding and effective organic pollutants degradation in water (Fig. 10). Wang *et al.* [233] described a phase-assisted degradation of BPA using α-MnO_2 doped with various facets of Cu in a PMS and full-spectrum light irradiation system. Three different Cu facets i.e. (100), (110), and (310) were prepared and doped on the α-MnO_2 to produce catalysts designated as Cu-doped(100)/PMS/light, Cu-doped(110)/PMS/light, Cu-doped (310)/PMS/light and pristine (110)/PMS/light system, respectively. The Cu-doped (110)/PMS/light system demonstrated the highest degradation efficiency of the BPA, with rich $^1O_2$ selectivity and generation, that is better than the rest of the phases and the pristine (110)/PMS/light counterpart. The associated pathway revealed that doping of α-MnO_2 with Cu improved light absorption, O_2 vacancies formation and electronic conductivity, in addition to activation of PMS. The Cu-doped(110)/PMS/light mineralized the organic pollutant, with 95% degradation efficiency of the TOC, and limited the harmfulness of the intermediates.

3.3.2. *Peroxydisulfate (PDS, $S_2O_8^{2-}$) and coupled systems*

The PDS with a greater redox potential than PMS (2.01 vs 1.82 V) [264] has also been activated with a CBC in AOPs towards the abatement of organic contaminants from water. Ma *et al.* [265] synthesized a two-metal organic framework (MIL-101(Fe/Cu) for coupled PS

Table 4
Reaction conditions and performance of peroxydisulfate-based catalysts in the degradation of organic pollutants

Reaction conditions						Efficiency of catalyst				
Catalyst	Contaminant	[C]	[Cu]	[PDS]	pH	[EoD](min)	k_{abs} (min^{-1})	[TOC] (min)	KRS	Reference
$CuFe_2O_4$/PDS NPs	p-NP	50 ppm	30 g/L	8 mmol/L	7	89% (60)	-	81%	$SO_4^{\bullet-}$	[267]
Fe_3Cu_2@NPC	TBBA	2.0 ppm	0.2 g/L	1 mM	10	100% (20)	0.2476	90 %	$O_2^{\bullet-}$	[268]
Cl^{-1}/Fe^{3+}/Cu^0/PDS	TC	5.0 ppm	1.0 μM	0.2 mM	3.0–7.0.	>96.5% (8 min)	0.406	-	$Cl^{\bullet}$, $SO_4^{\bullet-}$, and $^{\bullet}OH$	[269]
Fe2þ/CuO/PS system	ACT	100 ppm	CuO: 0.3 g/L Fe^{2+}: 0.07 mM	0.8 g/L	6.5	92% (90)	-	-	$SO_4^{\bullet-}$, and $^{\bullet}OH$	[270]
CuFeS2/PS/HA	CPF	20 ppm	0.9 g/L	0.6 mM	5	99% (80)	0.044	-	$^{\bullet}OH$	[266]
MIL-101(Fe/Cu (Fe to Cu molar ratio of 3:1)	TC	50 ppm	0.05 g/L.	2 mM	5	90.5%	0.0242	-	$SO_4^{\bullet-}$, $O_2^{\bullet-}$, $^{\bullet}OH$, and h^+	[271]

Keys: p-NP: p-nitrophenol; TBBA: Tetrabromobisphenol A; CPF: Chlorpyrifos.

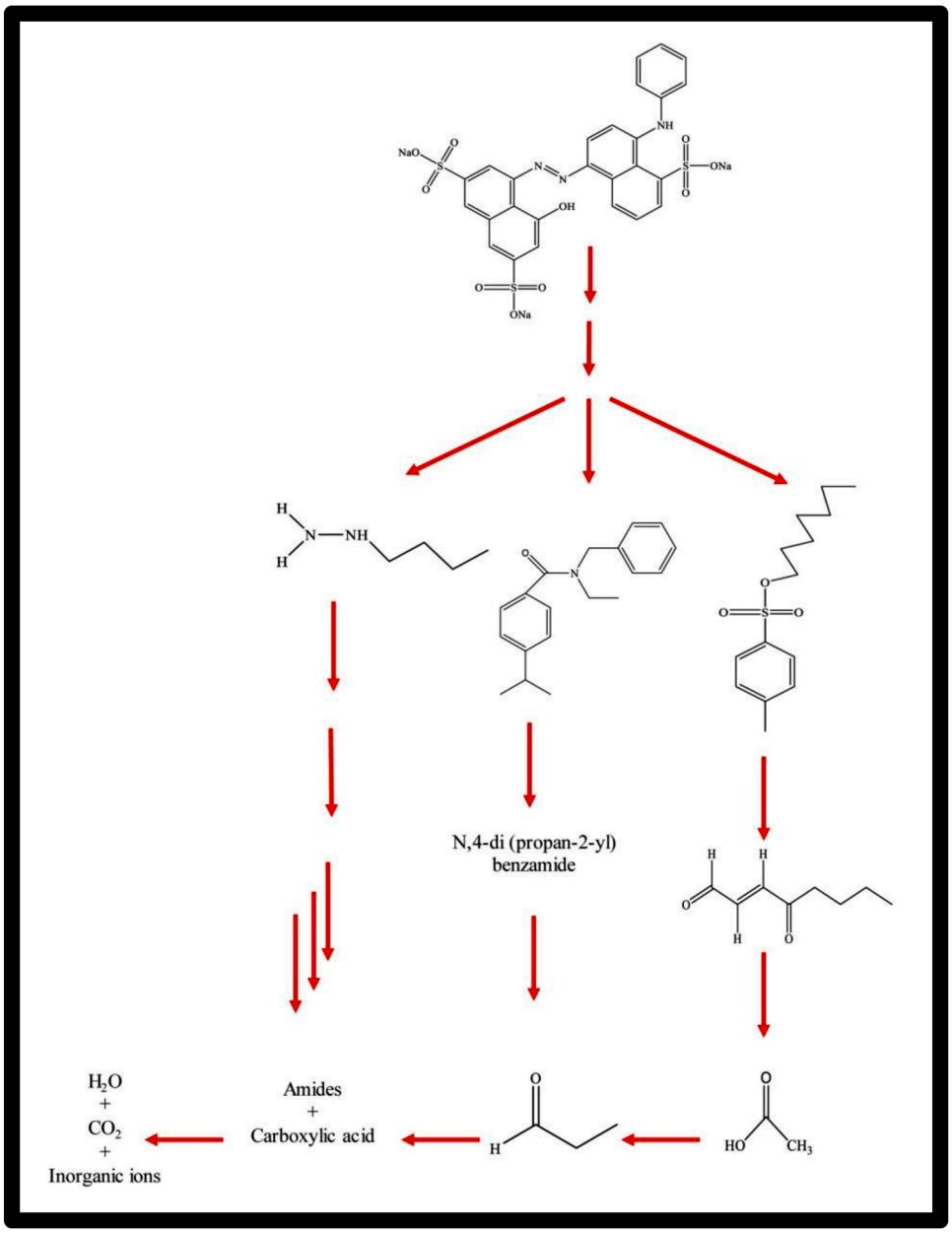

Fig. 11. The degradation pathway of the dye, AB 92, using the Cu_2O–CuO/HTC in a heterogeneous sonocatalysis. Figure reproduced from reference [292]. Copyright 2021 Elsevier.

oxidation and photocatalytic systems towards TC degradation. A degradation efficiency of 90.5% for 50 mg/L of TC was realized in the (MIL-101(Fe/Cu)/VL/PDS system; meanwhile 52.0% of equivalent TC concentration was removed in the MIL-101(Fe)/VL/PDS. The improved degradation of TC in the Cu-doped coupled PS oxidation and photocatalysis system can be attributed to several factors. These include the increased availability of stronger absorption energy (E_{abs}) to PDS, a reduction in the rate of recombination of e^--h^+ pair due to the capturing of photogenerated electrons by Cu, which limits e^--h^+ recombination. In addition, the improvement in electrical conductivity contributes to enhanced catalytic performance by increasing the catalyst's DOS (1.23 electron/eV). Successful degradation of organic contaminants has been reported for similar coupled systems using magnetic $Zn_{0.8}Cu_{0.2}$-Fe_2O_4/UV-vis light/PDS system in eco-friendly degradation of ATZ [252], Cu^+-decorated triazine-based g-C_3N_4 (Cu^+/g-C_3N_4) nanosheet-activated H_2O_2 for activation of PMS towards degradation of RhB [250], Cu-doped hematite nanoplates (named as CuHNPs)/PMS/VL for degradation of TC [255] and ultra-thin MOF (Cu-TCPP(BA)-MOF) with porphyrin/VL/PMS for the removal of RhB [67]; please see Table 4. The application of light was incredibly significant in acceleration of the transfer of electrons in the Cu^{2+}/Cu^+ redox circles. The activation of PS by the earth-abundant copper-iron sulfide mineral chalcopyrite ($CuFeS_2$) for the degradation of imidacloprid (IMP) and pesticide chlorpyrifos (CPF) in water was promoted by the addition of HA. The introduction of HA accelerated the regeneration of the Fe^{3+} and Cu^{2+} in the solution for PS decomposition [266].

3.3.3. *Percarbonate, peroxyacetic acid, and periodate*

Sodium percarbonate (SPC) has been used in the elimination of organic pollutants. For example, Liu and co-workers [272] reported the activation of SPC using micro-molar concentration levels of copper (II) towards orange 7 degradation where 97.5% could be removed within 15 mins. Another study has explored the use of CuO activated SPC in the presence of ascorbic acid where they studied the effect of pH on the

elimination of sulfamethazine (SMZ). The research demonstrated that the target pollutant could be degraded up to 86% at pH 9, with both Cu (III) species playing a significant role in the degradation mechanism [273]. Another notable work has reported the one-step hydrothermal synthesis of carrollite ($CuCo_2S_4$) for the activation of SPC directed towards bisphenol S (BPS) degradation [274]. The authors diligently studied the critical factors of pH, BPS concentration, $CuCo_2S_4$ dosage, SPC concentration, reaction temperature, water matrices, and inorganic anions. The results indicated that BPS can be degraded up to 88.5% at pH 6.9. The mechanism involved the degradation of BPS by $CuCo_2S_4$ activated by the SPC system, where a multiple ROS process was identified. This process included $^1O_2$, $O_2^{\bullet-}$, $^\bullet OH$, and carbonate ($CO_3^{\bullet-}$) radicals. Additionally, the sulfur species, S(-II), expedited rapid redox cycles between Cu(I)/Cu(II) and Co(II)/Co(III). The $CO_3^{\bullet-}$ not only directly reacted with BPS molecules, but also acted as a bridge to promote the generation of $^1O_2$ and $O_2^{\bullet-}$, thereby accelerating the degradation of BPS [274].

Peroxyacetic acid (PAA) also known as peracetic acid, is an organic peroxide-based colourless liquid with a low pH and a strong, pungent, and vinegar-like odour [275,276]. Zero valent copper has been used for the degradation of diclofenac, where PAA is activated to produce radicals that produce $^\bullet OH$, $CH_3COO^\bullet$ and $CH_3COOO^\bullet$ which are attributed to its catalytic decomposition [277]. Through the use of nanoparticle copper oxide, the degradation of CMZ has been reported within a neutral pH where the mechanism involves $CH_3C(O)OO^\bullet$ as the main dominant reactive species. [278] The use of PAA has been studied with cobalt, silver and copper ions as a catalyst where cobalt outperformed the use of silver and copper ions for the abatement of phenols [279]. This work suggests that researchers using exclusively CBC should focus on other activations. Periodate exists in different solid forms such as $NaIO_4$ (sodium metaperiodate), $Na_3H_2IO_6$ (sodium triparaperiodate, also named as trisodium dihydrogen orthoperiodate), KIO_4 (potassium metaperiodate), $Ba(IO_4)_2$ (barium periodate) and H_5IO_6 (orthoperiodic acid). Copper (III) periodate has been applied in the oxidation of substances such as glucitol and carbenicillin [280,281]. For a detailed overview, readers are encouraged to refer to the provided references [275,282].

3.4. Heterogeneous sonocatalytic degradation

Ultrasonic irradiation has become very significant in wastewater treatment and could be used in the abatement of organic contaminants such as herbicides, insecticides, pharmaceuticals, dyes, etc. [283]. Sonochemical methods employ ultrasound to generate an oxidative system through acoustic cavitation as a result of the rise and corresponding fall of microbubbles from compression/rarefaction induced by acoustical waves [284]. The bubble collapse produces a localized high temperature and pressure (hot-spots) conditions. The gases of a collapsing cavity can reach pressures up to 1000 atm and temperatures more than 5000 K within the collapsing cavity, with temperatures nearly reaching 1900 K in the interfacial area between collapsing bubble of the solution [285–289]. The organic contaminants are decomposed via two mechanisms:

i. The POPs within the cavity and around the interfacial regime (cavity-liquid) can go through thermal decomposition, involving combustion or pyrolysis reactions of O_2 during the implosion [289]. The significance of these hot-spots lies in the cleavage of H_2O molecules (into $^\bullet OH$ and $H^\bullet$ atom) and dissolved O_2 molecules (reactions (31), (32) [285–291]. Through the reactions of $H^\bullet$, $^\bullet OH$ and $O^\bullet$ with one another, as well as with O_2 and H_2O during the quick cooling phase, the H_2O_2 and $HO_2^\bullet$ radicals are generated [291].
ii. The hydroxyl radical and the homolytic oxygen are generated in the bubble during the rapid collapse [285–291]. These radicals either combine within the bubble (Eqs. 33–35) or leave the bubble, leading to the release of H_2O_2 into the system (Eqs. 36–38).

$$H_2O \rightarrow H^\bullet + {}^\bullet OH \quad (31)$$

$$O_2 \rightarrow 2O^\bullet \quad (32)$$

$$O^\bullet + H_2O \rightarrow 2{}^\bullet OH \quad (33)$$

$$H^\bullet + {}^\bullet OH \rightarrow H_2O \quad (34)$$

$$2{}^\bullet OH \rightarrow O^\bullet + H_2O \quad (35)$$

$$H^\bullet + O_2 \rightarrow HOO^\bullet \quad (36)$$

$$2{}^\bullet HO \rightarrow H_2O_2 \quad (37)$$

$$2HOO^\bullet \rightarrow H_2O_2 + O_2 \quad (38)$$

Reports have shown that with ultrasonic irradiation as a source of energy, e^- of M^{n+} can be excited from VB into CB, creating a h^+ by exceeding the E_g or aligning with the energy requirements of the catalyst. The generated h^+ can dislocate water molecules to form $^\bullet OH$ radicals, participating in the degradation of POPs in water. However, Cu_2O and CuO exhibit a lower quantum yield due to their high recombination rate and poor charge carrier mobility. To address this problem, heterogeneous sonocatalysis has been explored by researchers. For instance, Khataee and team [292] doped a high-yield and environmental friendly sawdust hydrochar, prepared by hydrothermal carbonization with Cu_2O-CuO (Cu_2O–CuO/HTC) at different carbonization times (2, 6, 12 h). This material demonstrated efficacy in the sonocatalytic decomposition of three dyes, namely, AB92, AR14, and AO7. Under optimal conditions, the Cu_2O–CuO/HTC-2h demonstrated the peak removal efficiency of 85.43% after 90 mins with a removal efficiency of 77.77%. Fig. 11 summarizes the decomposition pathway of the dye.

4. Factors influencing AOP

It is essential to highlight that the performance of the CBC in AOPs is a function of several factors, including: 1) temperature, since reaction rates in AOPs are often temperature-dependent. Elevated temperatures can enhance reaction kinetics, but excessively high temperatures may also lead to energy inefficiency or decreased stability of the reactants; 2) pH, which can significantly affect the efficiency of AOPs. Some AOPs are more effective under acidic or alkaline conditions and adjusting the pH to the optimal range for a specific AOP is crucial for achieving maximum degradation efficiency; 3) Concentration of reactive species, such as $^\bullet OH$, O_3, or other oxidizing agents, plays a critical role where optimizing the generation and concentration of these species is essential for efficient pollutant degradation; 4) type of AOP, which have distinct mechanisms and reactants. Common AOPs include photocatalysis (e.g., TiO_2 photocatalysis), ozonation, Fenton's reaction, and sonochemistry. The choice of AOP depends on the specific pollutants, water quality, and treatment objectives; 5) target pollutants, where the nature and concentration of pollutants in the water or air influence the selection of the AOP. Some AOPs may be more effective against certain types of pollutants, such as organic compounds, pathogens, or heavy metals; 6) reaction time, where the duration of exposure to the AOP is a crucial factor. Longer reaction times may lead to increased pollutant removal, but there is a trade-off with the energy consumption and practicality of the treatment process; 7) catalysts, such as semiconductor materials in photocatalysis or iron-based catalysts in Fenton's reaction, can enhance the efficiency of AOPs. Catalysts facilitate the generation of reactive species and promote the degradation of pollutants; 8) matrix effects, where the composition of the water matrix (e.g., presence of organic matter, ions, and other impurities) can influence the performance of AOPs. Some substances may compete for reactive species or scavenge radicals, affecting the overall degradation efficiency; 8) UV light availability, since AOPs like photocatalysis rely on the availability of UV or VL to activate catalysts. The intensity and wavelength of light can impact the effectiveness of the AOP, and consideration must be given to the light

source and its practical application; 9) safety and environmental impact, including the generation of by-products and potential risks, must be considered. Some AOPs may produce secondary pollutants, and their environmental sustainability should be assessed; 10) scale-up considerations where the feasibility of scaling up AOPs for practical applications in water treatment plants or industrial processes is a crucial factor. Factors such as reactor design, energy requirements, and cost-effectiveness need to be considered. In summary, understanding and optimizing these factors are essential for the successful application of AOPs in water and air treatment, helping to address environmental pollution challenges effectively.

5. Challenges and perspective

For more than ten decades now, a centralized municipal water purification process has been utilized, in an effort to provide safe water for communal use. However, growing concerns with these conventional water treatment processes necessitate a transition to more decentralized processes where AOPs might be competitive treatment alternatives. The use of heterogeneous catalysts has been pivotal in addressing the fundamental limitations that have constrained the practical application of typical AOPs, such as lowering their energy and chemical input requirements. Recent breakthroughs in the fabrication of advanced functional materials have been of tremendous benefit in engineering heterogeneous catalysts for applications in AOPs. From this perspective, the environmental impact of POPs was elucidated, while the properties and real-world applications of CBC in AOPs previously investigated, as well as reaction mechanisms and degradation pathways, were discussed in detail. The architecture and initial concentration of CBC, the initial dosage of the abated pollutant, the intensity of light, the surface chemistry and number of oxidation agents, the period of treatment, and the wastewater solution composition were all significant aspects of the AOPs. Without a doubt, the CBC exhibited exceptional catalytic performance in photocatalysis, Fenton-like processes, PS activation, and sonocatalytic processes, and could effectively abate organic pollutants from water via these AOPs. However, a few more issues are yet to be resolved, including:

i. The relatively high operational cost of these processes because of the employment of costly chemicals and higher energy requirements.
ii. The use of toxic CBC in some processes, which further poses an additional threat to the environment.
iii. The formation of unknown and in some cases, toxic intermediates that could be more harmful than the target pollutants.
iv. Scavenging of ROS radicals by non-target compounds.
v. Hindrances to large-scale production and requirement for highly skilled professionalism and associated costs.
vi. Difficulties in monitoring and maintaining reaction conditions in addition to monitoring water quality (e.g., chemicals, organic matter, and pH).
vii. Difficulty of removing H_2O_2, for example, from treated water.

Consequently, future investigations should involve step-by-step approach to lower resource and energy costs, environmental pollution, and employment of a cross-disciplinary approach involving science, engineering, technology, and artificial intelligence. This holistic approach is essential for addressing the whole challenge surrounding large-scale applications of copper-based heterogenous catalysts in AOPs.

CRediT authorship contribution statement

Enyioma C. Okpara: Writing – review & editing, Writing – original draft. **Olanrewaju B. Wojuola:** Writing – review & editing, Writing – original draft. **Taiwo W. Quadri:** Writing – review & editing, Writing – original draft. **Craig E. Banks:** Writing – review & editing, Writing – original draft.

Declaration of competing interest

The authors declare that they have no known competing financial interests or personal relationships that could have appeared to influence the work reported in this paper.

Data availability

No data was used for the research described in the article.

References

[1] W. Li, et al., In-situ growing of metal-organic frameworks on three-dimensional iron network as an efficient adsorbent for antibiotics removal, Chem. Eng. J. 392 (2020) 124844.
[2] Y. Yang, et al., In situ grown single-atom cobalt on polymeric carbon nitride with bidentate ligand for efficient photocatalytic degradation of refractory antibiotics, Small 16 (29) (2020) 2001634.
[3] Y. Yang, et al., Construction of iodine vacancy-rich BiOI/Ag@ AgI Z-scheme heterojunction photocatalysts for visible-light-driven tetracycline degradation: transformation pathways and mechanism insight, Chem. Eng. J. 349 (2018) 808–821.
[4] Q. He, et al., Peroxymonosulfate and peroxydisulfate activation by fish scales biochar for antibiotics removal: synergism of N, P-codoped biochar, Chemosphere 326 (2023) 138326.
[5] S. Chen, et al., In-situ synthesis of facet-dependent $BiVO_4/Ag_3PO_4$/PANI photocatalyst with enhanced visible-light-induced photocatalytic degradation performance: synergism of interfacial coupling and hole-transfer, Chem. Eng. J. 382 (2020) 122840.
[6] O. Lefebvre, R. Moletta, Treatment of organic pollution in industrial saline wastewater: a literature review, Water Res. 40 (20) (2006) 3671–3682.
[7] J.-L. Liu, M.-H. Wong, Pharmaceuticals and personal care products (PPCPs): a review on environmental contamination in China, Environ. Int. 59 (2013) 208–224.
[8] S. Tian, et al., Recent progress in sustainable technologies for adsorptive and reactive removal of sulfonamides, Chem. Eng. J. 389 (2020) 123423.
[9] Z. Liu, et al., Dual redox cycles of Mn(II)/Mn(III) and Mn(III)/Mn(IV) on porous Mn/N co-doped biochar surfaces for promoting peroxymonosulfate activation and ciprofloxacin degradation, J Colloid Interface Sci. 634 (2023) 255–267.
[10] B. Shao, et al., Disinfection byproducts formation from emerging organic micropollutants during chlorine-based disinfection processes, Chem. Eng. J. 455 (2023) 140476.
[11] E.D. Brown, G.D. Wright, Antibacterial drug discovery in the resistance era, Nature 529 (7586) (2016) 336–343.
[12] D.C. Muir, P.H. Howard, Are there other persistent organic pollutants? A challenge for environmental chemists, Environ. Sci. Technol. 40 (23) (2006) 7157–7166.
[13] B. Song, et al., Modeling the transport of sodium dodecyl benzene sulfonate in riverine sediment in the presence of multi-walled carbon nanotubes, Water Res. 129 (2018) 20–28.
[14] B. Shao, et al., The effects of biochar on antibiotic resistance genes (ARGs) removal during different environmental governance processes: a review, J. Hazard. Mater. 435 (2022) 129067.
[15] Y. Pan, et al., Activation of peroxydisulfate by bimetal modified peanut hull-derived porous biochar for the degradation of tetracycline in aqueous solution, J. Environ. Chem. Eng. 10 (2) (2022) 107366.
[16] T. Wu, et al., Tube wall delamination engineering induces photogenerated carrier separation to achieve photocatalytic performance improvement of tubular g-C_3N_4, J. Hazard. Mater. 424 (2022) 127177.
[17] X. Zhang, et al., Recent advances of Zr based metal organic frameworks photocatalysis: energy production and environmental remediation, Coord. Chem. Rev. 448 (2021) 214177.
[18] X. Zhou, et al., Persulfate activation by swine bone char-derived hierarchical porous carbon: multiple mechanism system for organic pollutant degradation in aqueous media, Chem. Eng. J. 383 (2020) 123091.
[19] W. Xiong, et al., Metal-organic frameworks derived magnetic carbon-αFe/Fe_3C composites as a highly effective adsorbent for tetracycline removal from aqueous solution, Chem. Eng. J. 374 (2019) 91–99.
[20] C. Zhang, et al., Efficacy of carbonaceous nanocomposites for sorbing ionizable antibiotic sulfamethazine from aqueous solution, Water Res. 95 (2016) 103–112.
[21] T. Wu, et al., Hydrogen peroxide-impregnated supramolecular precursors synthesize mesoporous-rich ant nest-like filled tubular g-C_3N_4 for effective photocatalytic removal of pollutants, Chem. Eng. J. 447 (2022) 137332.
[22] T. Wu, et al., Construction of a novel S-scheme heterojunction piezoelectric photocatalyst V-$BiOIO_3$/FTCN and immobilization with floatability for tetracycline degradation, J. Hazard. Mater. 443 (2023) 130251.
[23] B. Shao, et al., Application of carbon aerogel-based materials in persulfate activation for water treatment: a review, J. Clean. Prod. 384 (2023) 135518.

[24] M. Jia, et al., Integrating N and F co-doped TiO_2 nanotubes with ZIF-8 as photoelectrode for enhanced photo-electrocatalytic degradation of sulfamethazine, Chem. Eng. J. 388 (2020) 124388.
[25] M. Klavarioti, D. Mantzavinos, D. Kassinos, Removal of residual pharmaceuticals from aqueous systems by advanced oxidation processes, Environ. Int. 35 (2) (2009) 402–417.
[26] T.-Y. Tan, et al., Electrochemically enhanced simultaneous degradation of sulfamethoxazole, ciprofloxacin and amoxicillin from aqueous solution by multi-walled carbon nanotube filter, Sep. Purif. Technol. 235 (2020) 116167.
[27] Z.-z. Yang, et al., Design and engineering of layered double hydroxide based catalysts for water depollution by advanced oxidation processes: a review, J. Mater. Chem. A 8 (8) (2020) 4141–4173.
[28] T. Li, et al., Covalent–organic framework (COF)-core–shell composites: classification, synthesis, properties, and applications, Adv. Funct. Mater. 33 (45) (2023) 2304990.
[29] M.A. Oturan, J.-J. Aaron, Advanced oxidation processes in water/wastewater treatment: principles and applications. A review, Crit. Rev. Environ. Sci. Technol. 44 (23) (2014) 2577–2641.
[30] S. Ye, et al., Facile assembled biochar-based nanocomposite with improved graphitization for efficient photocatalytic activity driven by visible light, Appl. Catal. B 250 (2019) 78–88.
[31] H. Yi, et al., Synergistic effect of artificial enzyme and 2D nano-structured Bi_2WO_6 for eco-friendly and efficient biomimetic photocatalysis, Appl. Catal. B 250 (2019) 52–62.
[32] Y. Yang, et al., Recent advances in application of graphitic carbon nitride-based catalysts for degrading organic contaminants in water through advanced oxidation processes beyond photocatalysis: a critical review, Water Res. 184 (2020) 116200.
[33] X. Li, et al., A "bottle-around-ship" like method synthesized yolk-shell Ag3PO4@MIL-53 (Fe) Z-scheme photocatalysts for enhanced tetracycline removal, J Colloid Interface Sci. 561 (2020) 501–511.
[34] J.L. Wang, L.J. Xu, Advanced oxidation processes for wastewater treatment: formation of hydroxyl radical and application, Crit. Rev. Environ. Sci. Technol. 42 (3) (2012) 251–325.
[35] Y. Yang, et al., BiOX (X = Cl, Br, I) photocatalytic nanomaterials: applications for fuels and environmental management, Adv. Colloid Interface Sci. 254 (2018) 76–93.
[36] A. Saravanan, et al., A detailed review on advanced oxidation process in treatment of wastewater: mechanism, challenges and future outlook, Chemosphere 308 (2022) 136524.
[37] Y. Lin, et al., Gama-graphyne as photogenerated electrons transfer layer enhances photocatalytic performance of silver phosphate, Appl. Catal. B 264 (2020) 118479.
[38] Y. Liu, et al., Heterogeneous Fenton-like catalyst for treatment of rhamnolipid-solubilized hexadecane wastewater, Chemosphere 236 (2019) 124387.
[39] S. Wu, et al., High-performance porous carbon catalysts doped by iron and nitrogen for degradation of bisphenol F via peroxymonosulfate activation, Chem. Eng. J. 392 (2020) 123683.
[40] S. Anandan, S. Yang, Emergent methods to synthesize and characterize semiconductor CuO nanoparticles with various morphologies—an overview, J Exp Nanosci 2 (1–2) (2007) 23–56.
[41] Y. Li, et al., One-dimensional metal oxide nanotubes, nanowires, nanoribbons, and nanorods: synthesis, characterizations, properties and applications, Crit. Rev. Solid State Mater. Sci. 37 (1) (2012) 1–74.
[42] R. Narayanan, M.A. El-Sayed, Catalysis with Transition Metal Nanoparticles in Colloidal Solution: Nanoparticle Shape Dependence and Stability, ACS Publications, 2005, pp. 12663–12676.
[43] H. Zhang, et al., Facile synthesis of diverse transition metal oxide nanoparticles and electrochemical properties, Inorg. Chem. Front. 3 (8) (2016) 1048–1057.
[44] Y. Xu, M.A. Schoonen, The absolute energy positions of conduction and valence bands of selected semiconducting minerals, Am. Mineral. 85 (3–4) (2000) 543–556.
[45] S. Sun, et al., Tuning interfacial Cu-O atomic structures for enhanced catalytic applications, Chemistry, 14 (17) (2019) 2912–2924.
[46] K.Y. Kumar, et al., Hydrothermal synthesis of hierarchical copper oxide nanoparticles and its potential application as adsorbent for Pb (II) with high removal capacity, Sep. Sci. Technol. 49 (15) (2014) 2389–2399.
[47] M. Nesa, et al., Structural, optical and electronic properties of CuO and Zn doped CuO: DFT based First-principles calculations, Chem. Phys. 528 (2020) 110536.
[48] P. Raizada, et al., Engineering nanostructures of CuO-based photocatalysts for water treatment: current progress and future challenges, Arab. J. Chem. 13 (11) (2020) 8424–8457.
[49] S. Chandrasekaran, et al., Recent advances in metal sulfides: from controlled fabrication to electrocatalytic, photocatalytic and photoelectrochemical water splitting and beyond, Chem. Soc. Rev. 48 (15) (2019) 4178–4280.
[50] Y. Zhang, H. Xu, Q. Wang, Ultrathin single crystal ZnS nanowires, Chem. Commun. 46 (47) (2010) 8941–8943.
[51] Q. Zhao, et al., Spinels: controlled preparation, oxygen reduction/evolution reaction application, and beyond, Chem. Rev. 117 (15) (2017) 10121–10211.
[52] E.C. Okpara, et al., Applications of transition metal oxides and chalcogenides and their composites in water treatment: a review, Environ. Adv. 11 (2023) 100341.
[53] Y. Li, et al., Recent advances in waste water treatment through transition metal sulfides-based advanced oxidation processes, Water Res. 192 (2021) 116850.
[54] M. Chauhan, K. Soni, P.E. Karthik, K.P. Reddy, C.S. Gopinath, S. Deka, Promising visible-light driven hydrogen production from water on a highly efficient $CuCo_2S_4$ nanosheet photocatalyst, J. Mater. Chem. A 7 (12) (2019) 6985–6994.
[55] J.-N. Zhu, et al., Preparing copper doped carbon nitride from melamine templated crystalline copper chloride for Fenton-like catalysis, Appl. Catal. B 256 (2019) 117830.
[56] Y. Li, T. Kong, S. Shen, Artificial photosynthesis with polymeric carbon nitride: when meeting metal nanoparticles, single atoms, and molecular complexes, Small 15 (32) (2019) 1900772.
[57] X. Zhou, et al., Identification of Fenton-like active Cu sites by heteroatom modulation of electronic density, Proc. Natl. Acad. Sci. 119 (8) (2022) e2119492119.
[58] Y. Chao, C. Yan, J. Gu, Y. Zhang, X. Li, Z. Dang, L. Wang, J. Wan, J. Pan, In-situ Cu-loaded sludge biochar catalysts for oxidative degradation of bisphenol A from high-salinity wastewater, J. Clean Prod. 427 (2023) 139334.
[59] Y. Zhu, et al., Strategies for enhancing the heterogeneous Fenton catalytic reactivity: a review, Appl. Catal. B 255 (2019) 117739.
[60] M. Fang, et al., CuO nanosheet as a recyclable Fenton-like catalyst prepared from simulated Cu(II) waste effluents by alkaline H_2O_2 reaction, Environ. Sci. 6 (1) (2019) 105–114.
[61] J. Zhu, et al., A high-efficiency CuO/CeO_2 catalyst for diclofenac degradation in Fenton-like system, Front. Chem. 7 (2019) 796.
[62] M. Silva, et al., Heterogeneous photo-Fenton-like degradation of emerging pharmaceutical contaminants in wastewater using Cu-doped MgO nanoparticles, Appl. Catal. A 630 (2022) 118468.
[63] H. Li, et al., Design and synthesis of an exceptionally stable and highly porous metal-organic framework, Nature 402 (6759) (1999) 276–279.
[64] M. Zhang, et al., Symmetry-guided synthesis of highly porous metal–organic frameworks with fluorite topology, Angew. Chem. 126 (3) (2014) 834–837.
[65] Y. Cui, et al., Luminescent functional metal–organic frameworks, Chem. Rev. 112 (2) (2012) 1126–1162.
[66] L. Pan, et al., A resistance-switchable and ferroelectric metal–organic framework, J. Am. Chem. Soc. 136 (50) (2014) 17477–17483.
[67] Y. Bai, et al., Cu-MOF for effectively organic pollutants degradation and E. coli inactivation via catalytic activation of peroxymonosulfate, J. Taiwan Inst. Chem. Eng. 132 (2022) 104154.
[68] Q. Wang, et al., Ultrasound-enhanced zero-valent copper activation of persulfate for the degradation of bisphenol AF, Chem. Eng. J. 378 (2019) 122143.
[69] X. Ma, et al., Ultrasound-enhanced nanosized zero-valent copper activation of hydrogen peroxide for the degradation of norfloxacin, Ultrason. Sonochem. 40 (2018) 763–772.
[70] X. Liu, et al., Rapid oxidation of acetaminophen with zero-valent copper induced hydrogen peroxide process in presence of ferric ion and chloride ion, Chem. Eng. J. 470 (2023) 144202.
[71] X. Liu, et al., Multiple reinforcement of chloride ion on oxidizing acetaminophen with zero-valent copper particles: in-site formation and catalysis of hydrogen peroxide, Chem. Eng. J. 451 (2023) 138689.
[72] Z. Sharifi, G. Asgari, A. Seid-Mohammadi, Sonocatalytic degradation of p-chlorophenol by nanoscale zero-valent copper activated persulfate under ultrasonic irradiation in aqueous solutions, Int. J. Eng. 33 (6) (2020) 1061–1069.
[73] H. Lu, et al., Efficient degradation of nitrobenzene by Cu-Co-Fe-LDH catalyzed peroxymonosulfate to produce hydroxyl radicals, Chem. Eng. J. 357 (2019) 140–149.
[74] D. Li, et al., Persulfate coupled with Cu^{2+}/LDH-MoS_4: a novel process for the efficient atrazine abatement, mechanism and degradation pathway, Chem. Eng. J. 436 (2022) 134933.
[75] Y. Guo, P. Qi, Y. Liu, A review on advanced treatment of pharmaceutical wastewater, in: IOP Conference Series: Earth and Environmental Science, IOP Publishing, 2017.
[76] A.G. Prado, L.L. Costa, Photocatalytic decouloration of malachite green dye by application of TiO_2 nanotubes, J. Hazard. Mater. 169 (1–3) (2009) 297–301.
[77] C. Chen, et al., UV light induced photodegradation of malachite green on TiO_2 nanoparticles, J. Hazard. Mater. 141 (3) (2007) 520–528.
[78] L. Saikia, et al., Photocatalytic performance of ZnO nanomaterials for self sensitized degradation of malachite green dye under solar light, Appl. Catal. A 490 (2015) 42–49.
[79] S.C. Ameta, R. Ameta, Advanced Oxidation Processes for Wastewater Treatment: Emerging Green Chemical Technology, Academic Press, 2018.
[80] Z. Huang, et al., Facile synthesis of S-doped reduced TiO_2-x with enhanced visible-light photocatalytic performance, Chin. J. Catal. 38 (5) (2017) 821–830.
[81] J.-J. Huang, C.-C. Lin, D.-S. Wuu, Antireflection and passivation property of titanium oxide thin film on silicon nanowire by liquid phase deposition, Surf. Coat. Technol. 320 (2017) 252–258.
[82] K. Micheal, et al., Assembled composite of hematite iron oxide on sponge-like BiOCl with enhanced photocatalytic activity, Mater. Sci. Energy Technol. 2 (1) (2019) 104–111.
[83] Y.-H. Chiu, et al., Mechanistic insights into photodegradation of organic dyes using heterostructure photocatalysts, Catalysts 9 (5) (2019) 430.
[84] X. Li, et al., TiO_2 nanoparticles assembled on kaolinites with different morphologies for efficient photocatalytic performance, Sci. Rep. 8 (1) (2018) 11663.
[85] B. Ünlü, S. Çakar, M. Özacar, The effects of metal doped TiO_2 and dithizone-metal complexes on DSSCs performance, Sol. Energy 166 (2018) 441–449.
[86] L. Zhang, M. Jaroniec, Toward designing semiconductor-semiconductor heterojunctions for photocatalytic applications, Appl. Surf. Sci. 430 (2018) 2–17.
[87] S.C. Priya, et al., A critical review on efficient photocatalytic degradation of organic compounds using copper-based nanoparticles, Mater. Today 80 (2023) 3075–3081.

[88] M.Z. Ansari, et al., Highly dispersible and uniform size Cu_2ZnSnS_4 nanoparticles for photocatalytic application, Adv. Powder Technol. 28 (9) (2017) 2402–2409.
[89] D.P. Das, et al., Solar-light induced photodegradation of organic pollutants over CdS-pillared zirconium–titanium phosphate (ZTP), J. Mol. Catal. A 349 (1) (2011) 36–41.
[90] Z. Zhou, et al., Microwave fabrication of Cu_2ZnSnS_4 nanoparticle and its visible light photocatalytic properties, Nanoscale Res. Lett. 9 (2014) 1–6.
[91] S.A. Phaltane, et al., Photocatalytic degradation of methylene blue by hydrothermally synthesized CZTS nanoparticles, J. Mater. Sci. 28 (2017) 8186–8191.
[92] M. Sampath, et al., Structural, optical and photocatalytic properties of spray deposited Cu_2ZnSnS_4 thin films with various S/(Cu+Zn+Sn) ratio, Mater. Sci. Semicond. Process. 87 (2018) 54–64.
[93] Q. Xu, et al., Synthesis of hierarchical Cu_2CdSnS_4 by microwave-assisted transformation from precursor for photodegradation to malachite green, J. Alloys Compd. 904 (2022) 163966.
[94] H. Karimi-Maleh, et al., The role of magnetite/graphene oxide nano-composite as a high-efficiency adsorbent for removal of phenazopyridine residues from water samples, an experimental/theoretical investigation, J. Mol. Liq. 298 (2020) 112040.
[95] Y. Orooji, et al., Recent advances in nanomaterial development for lithium ion-sieving technologies, Desalination 529 (2022) 115624.
[96] J.K. Patra, et al., Proteasome inhibitory, antioxidant, and synergistic antibacterial and anticandidal activity of green biosynthesized magnetic Fe_3O_4 nanoparticles using the aqueous extract of corn (Zea mays L.) ear leaves, Artif. Cells Nanomed. Biotechnol. 45 (2) (2017) 349–356.
[97] A. Ramesh, et al., Facile green synthesis of Fe_3O_4 nanoparticles using aqueous leaf extract of Zanthoxylum armatum DC. for efficient adsorption of methylene blue, J. Asian Ceram. Soc. 6 (2) (2018) 145–155.
[98] C. Prasad, et al., Bio inspired green synthesis of Ni/Fe_3O_4 magnetic nanoparticles using *Moringa oleifera* leaves extract: a magnetically recoverable catalyst for organic dye degradation in aqueous solution, J. Alloys Compd. 700 (2017) 252–258.
[99] N.F. Takmil, et al., Hydrogen production by electrochemical reaction using waste zeolite boosted with titania and Au nanoparticles, Inorg. Chem. Commun. 133 (2021) 108891.
[100] D. Habibi, M. Nasrollahzadeh, H. Sahebekhtiari, Green synthesis of formamides using the Natrolite zeolite as a natural, efficient and recyclable catalyst, J. Mol. Catal. A 378 (2013) 148–155.
[101] M. Nasrollahzadeh, et al., Recent progresses in the application of cellulose, starch, alginate, gum, pectin, chitin and chitosan based (nano) catalysts in sustainable and selective oxidation reactions: a review, Carbohydr. Polym. 241 (2020) 116353.
[102] M. Sajjadi, et al., Lignin-derived (nano) materials for environmental pollution remediation: current challenges and future perspectives, Int. J. Biol. Macromol. 178 (2021) 394–423.
[103] S. Byun, et al., Mechanistic studies of magnetically recyclable Pd–Fe_3O_4 heterodimeric nanocrystal-catalyzed organic reactions, Chemistry, 10 (4) (2015) 982–988.
[104] Z. Cheng, J. Meng, X. Wang, Preparation of wood-based filter loaded with Ag nanoparticles and its catalytic degradation performance on organic dye, J. For. Eng 5 (2020) 94–98.
[105] Y. Orooji, K. Pakzad, M. Nasrollahzadeh, Lignosulfonate valorization into a Cu-containing magnetically recyclable photocatalyst for treating wastewater pollutants in aqueous media, Chemosphere 305 (2022) 135180.
[106] C.N.R. Rao, et al., Graphene: the new two-dimensional nanomaterial, Angew. Chem. Int. Ed. 48 (42) (2009) 7752–7777.
[107] C.W. Bielawski, et al., The chemistry of grapheme oxide, Chem. Soc. Rev. 39 (1) (2010) 228–240.
[108] A.K. Geim, Graphene: status and prospects, Science 324 (5934) (2009) 1530–1534.
[109] M.J. Allen, V.C. Tung, R.B. Kaner, Honeycomb carbon: a review of graphene, Chem. Rev. 110 (1) (2010) 132–145.
[110] J.S. Bunch, et al., Electromechanical resonators from graphene sheets, Science 315 (5811) (2007) 490–493.
[111] A.A. Balandin, et al., Superior thermal conductivity of single-layer graphene, Nano Lett. 8 (3) (2008) 902–907.
[112] Z. Jin, et al., Fabrication of efficient visible light activated Cu–P25–graphene ternary composite for photocatalytic degradation of methyl blue, Appl. Surf. Sci. 356 (2015) 707–718.
[113] C.-C. Lin, Y.-J. Chiang, Preparation of coupled ZnO/SnO_2 photocatalysts using a rotating packed bed, Chem. Eng. J. 181 (2012) 196–205.
[114] J. Zeng, et al., Hydrothermal synthesis and photocatalytic properties of pyrochlore $La_2Sn_2O_7$ nanocubes, J. Phys. Chem. C 111 (32) (2007) 11879–11887.
[115] Y. Duan, et al., Morphology engineering of ZnO nanostructures for enhanced photocatalytic efficiency of In $(OH)_3$/ZnO nanocomposite, Appl. Surf. Sci. 535 (2021) 147657.
[116] F. Yousefzadeh, M. Ghanbari, M. Salavati-Niasari, Sonochemical synthesis and characterization of Sm_2CuO_4 nanostructures and their application as visible-light photocatalyst for degradation of water-soluble organic pollutants, Chemosphere 338 (2023) 139564.
[117] E.C. Okpara, et al., Green wastes mediated zinc oxide nanoparticles: synthesis, characterization and electrochemical studies, Materials 13 (19) (2020) 4241.
[118] Y. Yulizar, D.O.B. Apriandanu, R.I. Ashna, La_2CuO_4-decorated ZnO nanoparticles with improved photocatalytic activity for malachite green degradation, Chem. Phys. Lett. 755 (2020) 137749.
[119] M. Sampath, et al., Structural, optical and photocatalytic properties of spray deposited Cu_2ZnSnS_4 thin films with various S/(Cu+ Zn+ Sn) ratio, Mater. Sci. Semicond. Process. 87 (2018) 54–64.
[120] Y. Hunge, et al., Visible light assisted photoelectrocatalytic degradation of sugarcane factory wastewater by sprayed CZTS thin films, J. Phys. Chem. Solids 111 (2017) 176–181.
[121] A. Muthuvel, M. Jothibas, C. Manoharan, Synthesis of copper oxide nanoparticles by chemical and biogenic methods: photocatalytic degradation and in vitro antioxidant activity, Nanotechnol. Environ. Eng. 5 (2020) 1–19.
[122] H. Zangeneh, M. Farhadian, A.A. Zinatizadeh, N (Urea) and CN (L-Asparagine) doped TiO_2-CuO nanocomposites: fabrication, characterization and photodegradation of direct red 16, J. Environ. Chem. Eng. 8 (1) (2020) 103639.
[123] R.G. Saratale, et al., Photocatalytic activity of CuO/Cu $(OH)_2$ nanostructures in the degradation of reactive Green 19A and textile effluent, phytotoxicity studies and their biogenic properties (antibacterial and anticancer), J. Environ. Manag. 223 (2018) 1086–1097.
[124] D. Jiang, et al., Photocatalytic performance enhancement of CuO/Cu_2O heterostructures for photodegradation of organic dyes: effects of CuO morphology, Appl. Catal. B 211 (2017) 199–204.
[125] A.-J. Simamora, et al., Photocatalytic splitting of seawater and degradation of methylene blue on CuO/nano TiO_2, Int. J. Hydrogen Energy 37 (18) (2012) 13855–13858.
[126] R. Chen, et al., Synthesis of CuO/Co_3O_4 coaxial heterostructures for efficient and recycling photodegradation, Int. J. Photoenergy 2015 (2015) 1–11.
[127] Z. Yu, et al., Heterostructured metal oxides-ZnO nanorods films prepared by SPPS route for photodegradation applications, Surf. Coat. Technol. 375 (2019) 670–680.
[128] K. Salehi, et al., Response surface methodology (RSM) optimization approach for degradation of direct Blue 71 dye using CuO–ZnO nanocomposite, Int. J. Environ. Sci. Technol. 14 (2017) 2067–2076.
[129] M.B. Fisher, et al., Nitrogen and copper doped solar light active TiO_2 photocatalysts for water decontamination, Appl. Catal. B 130 (2013) 8–13.
[130] K. Mageshwari, et al., Novel $CuCr_2O_4$ embedded CuO nanocomposites for efficient photodegradation of organic dyes, Appl. Surf. Sci. 353 (2015) 95–102.
[131] E. Alzahrani, Chitosan membrane embedded with ZnO/CuO nanocomposites for the photodegradation of fast green dye under artificial and solar irradiation, Anal. Chem. Insights 13 (2018) 1–13, 1177390118763361.
[132] A. Arshad, et al., Solar light triggered catalytic performance of graphene-CuO nanocomposite for waste water treatment, Ceram. Int. 43 (14) (2017) 10654–10660.
[133] S. Mosleh, et al., Sonochemical-assisted synthesis of CuO/Cu_2O/Cu nanoparticles as efficient photocatalyst for simultaneous degradation of pollutant dyes in rotating packed bed reactor: LED illumination and central composite design optimization, Ultrason. Sonochem. 40 (2018) 601–610.
[134] J. Ding, et al., Low-temperature preparation of magnetically separable Fe_3O_4@ CuO-RGO core-shell heterojunctions for high-performance removal of organic dye under visible light, J. Alloys Compd. 688 (2016) 649–656.
[135] Y. Kanigaridou, et al., Solar photocatalytic degradation of bisphenol A with CuOx/$BiVO_4$: insights into the unexpectedly favorable effect of bicarbonates, Chem. Eng. J. 318 (2017) 39–49.
[136] M. Mureseanu, et al., Green synthesis of g-C_3N_4/CuONP/LDH composites and derived g-C_3N_4/MMO and their photocatalytic performance for phenol reduction from aqueous solutions, Appl. Clay Sci. 141 (2017) 1–12.
[137] T. Sun, et al., Efficient degradation of p-arsanilic acid with arsenic adsorption by magnetic CuO-Fe_3O_4 nanoparticles under visible light irradiation, Chem. Eng. J. 334 (2018) 1527–1536.
[138] A. Nezamzadeh-Ejhieh, M. Amiri, CuO supported clinoptilolite towards solar photocatalytic degradation of p-aminophenol, Powder Technol. 235 (2013) 279–288.
[139] P. Ma, et al., Ag3PO4/CuO composites utilizing the synergistic effect of photocatalysis and Fenton-like catalysis to dispose organic pollutants, Adv. Powder Technol. 28 (11) (2017) 2797–2804.
[140] S. Hong, et al., Highly efficient and recyclable g-C_3N_4/CuO hybrid nanocomposite towards enhanced visible-light photocatalytic performance, Nano 11 (11) (2016) 1650121.
[141] D. Wang, et al., Construction of ternary annular 2Z-scheme+ 1Heterojunction CuO/WO_3/CdS/photocatalytic system for methylene blue degradation with simultaneous hydrogen production, Appl. Surf. Sci. 498 (2019) 143843.
[142] C. Wu, et al., Fabrication of CuS/CuO nanowire heterostructures on copper mesh with improved visible light photocatalytic properties, J. Phys. Chem. Solids 140 (2020) 109355.
[143] E. Kamaraj, et al., Facile fabrication of CuO-Pb_2O_3 nanophotocatalyst for efficient degradation of Rose Bengal dye under visible light irradiation, Appl. Surf. Sci. 433 (2018) 206–212.
[144] M. Ranjeh, et al., Pechini sol–gel synthesis of Cu_2O/Li_3BO_3 and CuO/Li_3BO_3 nanocomposites for visible light-driven photocatalytic degradation of dye pollutant, J. Alloys Compd. 815 (2020) 152451.
[145] S.M. Tabatabaeinejad, et al., $Dy_2Cu_2O_5$ nanostructures: sonochemical fabrication, characterization, and investigation of photocatalytic ability for elimination of organic contaminants, J. Mol. Liq. 344 (2021) 117883.
[146] R. Rahmatolahzadeh, S.A. Shobeiri, K. Motevalli, Synthesis, characterization, and morphological control of $Cn_3B_2O_6$ nanostructures by sol–gel process for azo dye degradation, J. Mater. Sci. 29 (2018) 4327–4333.
[147] S. Luo, et al., Enhancement of visible-light photocatalytic activity of $Cu_3B_2O_6$ hybridized with g-C_3N_4, Colloids Surf. A 520 (2017) 409–419.

[148] V.T. Quyen, et al., Enhanced the visible light photocatalytic decomposition of antibiotic pollutant in wastewater by using Cu doped WO_3, J. Environ. Chem. Eng. 9 (1) (2021) 104737.
[149] R. Rahmatolahzadeh, M. Mousavi-Kamazani, S.A. Shobeiri, Facile co-precipitation-calcination synthesis of $CuCo_2O_4$ nanostructures using novel precursors for degradation of azo dyes, J. Inorg. Organomet. Polym. Mater. 27 (2017) 313–322.
[150] S. Wojtyła, W. Macyk, T. Baran, Photosensitization of CuI–the role of visible light induced CuI → CuII transition in photocatalytic degradation of organic pollutants and inactivation of microorganisms, Photochem. Photobiol. Sci. 16 (7) (2017) 1079–1087.
[151] S.M. Tabatabaeinejad, et al., Facile sonochemical preparation of $La_2Cu_2O_5$ nanostructures, characterization, the evaluation of performance, mechanism, and kinetics of photocatalytic reactions for the removal of toxic pollutants, J. Mol. Liq. 362 (2022) 119718.
[152] N.T.T. Truc, et al., The advanced photocatalytic degradation of atrazine by direct Z-scheme Cu doped ZnO/g-C_3N_4, Appl. Surf. Sci. 489 (2019) 875–882.
[153] C. Yang, C. Zhang, L. Liu, Excellent degradation performance of 3D hierarchical nanoporous structures of copper towards organic pollutants, J. Mater. Chem. A 6 (42) (2018) 20992–21002.
[154] S.M. Tabatabaeinejad, et al., Magnetic $Lu_2Cu_2O_5$-based ceramic nanostructured materials fabricated by a simple and green approach for an effective photocatalytic degradation of organic contamination, RSC Adv., 11 (63) (2021) 40100–40111.
[155] H. Safajou, et al., Green synthesis and characterization of RGO/Cu nanocomposites as photocatalytic degradation of organic pollutants in waste-water, Int. J. Hydrogen Energy 46 (39) (2021) 20534–20546.
[156] G. Gogoi, et al., Iron and copper catalysts derived from inorganic waste for dye degradation, ChemistrySelect 8 (27) (2023) e202300279.
[157] M. Zhang, et al., Highly efficient decomposition of organic dye by aqueous-solid phase transfer and in situ photocatalysis using hierarchical copper phthalocyanine hollow spheres, ACS Appl. Mater. Interfaces 3 (7) (2011) 2573–2578.
[158] V. Kumari, et al., Surface Plasmon response of Pd deposited ZnO/CuO nanostructures with enhanced photocatalytic efficacy towards the degradation of organic pollutants, Inorg. Chem. Commun. 121 (2020) 108241.
[159] H.R. Mardani, et al., Visible light photo-degradation of methylene blue over Fe or Cu promoted ZnO nanoparticles, Spectrochim. Acta Part A 141 (2015) 27–33.
[160] E. Akbarzadeh, et al., Preparation and characterization of novel Ag_3VO_4/Cu-MOF/rGO heterojunction for photocatalytic degradation of organic pollutants, Mater. Res. Bull. 121 (2020) 110621.
[161] N. Ahmadpour, et al., A potential natural solar light active photocatalyst using magnetic $ZnFe_2O_4$@ TiO_2/Cu nanocomposite as a high performance and recyclable platform for degradation of naproxen from aqueous solution, J. Clean. Prod. 268 (2020) 122023.
[162] M. Sorbiun, et al., Green synthesis of zinc oxide and copper oxide nanoparticles using aqueous extract of oak fruit hull (Jaft) and comparing their photocatalytic degradation of basic violet 3, Int. J. Environ. Res. 12 (2018) 29–37.
[163] L. He, et al., Cu_2MoS_4-based magnetic composites as effective adsorbent and photocatalyst for removal of organic contaminants in water, J. Taiwan Inst. Chem. Eng. 127 (2021) 312–326.
[164] N.T. Hanh, et al., Monocrotophos pesticide effectively removed by novel visible light driven Cu doped ZnO photocatalyst, J. Photochem. Photobiol. A 382 (2019) 111923.
[165] J. Esmaili-Hafshejani, A. Nezamzadeh-Ejhieh, Increased photocatalytic activity of Zn (II)/Cu (II) oxides and sulfides by coupling and supporting them onto clinoptilolite nanoparticles in the degradation of benzophenone aqueous solution, J. Hazard. Mater. 316 (2016) 194–203.
[166] J. Wang, et al., A high efficient photocatalyst Ag_3VO_4/TiO_2/graphene nanocomposite with wide spectral response, Appl. Catal. B 136 (2013) 94–102.
[167] S. Ameen, et al., Solution-processed CeO_2/TiO_2 nanocomposite as potent visible light photocatalyst for the degradation of bromophenol dye, Chem. Eng. J. 247 (2014) 193–198.
[168] S. Pany, K. Parida, A facile in situ approach to fabricate N, S-TiO_2/gC_3N_4 nanocomposite with excellent activity for visible light induced water splitting for hydrogen evolution, Phys. Chem. Chem. Phys. 17 (12) (2015) 8070–8077.
[169] D. Jiang, et al., Distinguishing localized surface plasmon resonance and schottky junction of Au–Cu_2O composites by their molecular spacer dependence, ACS Appl. Mater. Interfaces 6 (14) (2014) 10958–10962.
[170] C.-H. Kuo, et al., Facet-dependent and Au nanocrystal-enhanced electrical and photocatalytic properties of Au—Cu_2O core—shell heterostructures, J. Am. Chem. Soc. 133 (4) (2011) 1052–1057.
[171] L. Li, et al., Pd-Cu_2O and Ag-Cu_2O Hybrid Concave Nanomaterials for an Effective Synergistic Catalyst, Angew. Chem. Int. Ed. 52 (42) (2013) 11049–11053.
[172] R. Deng, et al., Biochar-mediated Fenton-like reaction for the degradation of sulfamethazine: role of environmentally persistent free radicals, Chemosphere 255 (2020) 126975.
[173] J. Li, et al., Recent advances in Cu-Fenton systems for the treatment of industrial wastewaters: role of Cu complexes and Cu composites, J. Hazard. Mater. 392 (2020) 122261.
[174] J.J. Pignatello, E. Oliveros, A. MacKay, Advanced oxidation processes for organic contaminant destruction based on the Fenton reaction and related chemistry, Crit. Rev. Environ. Sci. Technol. 36 (1) (2006) 1–84.
[175] P. Gholami, A. Khataee, A. Bhatnagar, Environmentally superior cleaning of diatom frustules using sono-Fenton process: facile fabrication of nanoporous silica with homogeneous morphology and controlled size, Ultrason. Sonochem. 64 (2020) 105044.
[176] C. von Sonntag, et al., The fate of peroxyl radicals in aqueous solution, Water Sci. Technol. 35 (4) (1997) 9–15.
[177] G.V. Buxton, et al., Critical Review of rate constants for reactions of hydrated electrons, hydrogen atoms and hydroxyl radicals (· OH/· O− in Aqueous Solution, J. Phys. Chem. Ref. Data 17 (2) (1988) 513–886.
[178] M. Cheng, et al., Efficient degradation of sulfamethazine in simulated and real wastewater at slightly basic pH values using Co-SAM-SCS /H2O2 Fenton-like system, Water Res. 138 (2018) 7–18.
[179] D. Huang, et al., Nonnegligible role of biomass types and its compositions on the formation of persistent free radicals in biochar: insight into the influences on Fenton-like process, Chem. Eng. J. 361 (2019) 353–363.
[180] L. Li, et al., Degradation of naphthalene with magnetic bio-char activate hydrogen peroxide: synergism of bio-char and Fe–Mn binary oxides, Water Res. 160 (2019) 238–248.
[181] J. Ma, et al., Stable cuprous active sites in Cu+-graphitic carbon nitride: structure analysis and performance in Fenton-like reactions, J. Hazard. Mater. 378 (2019) 120782.
[182] M.B. Gawande, et al., Cu and Cu-based nanoparticles: synthesis and applications in catalysis, Chem. Rev. 116 (6) (2016) 3722–3811.
[183] D.A. Nichela, et al., Nitrobenzene degradation in Fenton-like systems using Cu (II) as catalyst. Comparison between Cu (II)-and Fe (III)-based systems, Chem. Eng. J. 228 (2013) 1148–1157.
[184] L. Lyu, et al., Enhanced Fenton catalytic efficiency of γ-Cu-Al_2O_3 by σ-Cu2+− ligand complexes from aromatic pollutant degradation, Environ. Sci. Technol. 49 (14) (2015) 8639–8647.
[185] L. Zhang, et al., Framework Cu-doped $AlPO_4$ as an effective Fenton-like catalyst for bisphenol A degradation, Appl. Catal. B 207 (2017) 9–16.
[186] L. Lyu, et al., Efficient destruction of pollutants in water by a dual-reaction-center Fenton-like process over carbon nitride compounds-complexed Cu (II)-$CuAlO_2$, Environ. Sci. Technol. 52 (7) (2018) 4294–4304.
[187] S. Chu, et al., Band structure engineering of carbon nitride: in search of a polymer photocatalyst with high photooxidation property, ACS Catal. 3 (5) (2013) 912–919.
[188] L. Lyu, et al., 4-phenoxyphenol-functionalized reduced graphene oxide nanosheets: a metal-free Fenton-like catalyst for pollutant destruction, Environ. Sci. Technol. 52 (2) (2018) 747–756.
[189] J. Li, et al., Synthesis and internal electric field dependent photoreactivity of Bi3O4Cl single-crystalline nanosheets with high {001} facet exposure percentages, Nanoscale 6 (1) (2014) 167–171.
[190] L. Zhang, Y. Su, W. Wang, Internal electric fields within the photocatalysts, Prog. Chem. 28 (4) (2016) 415.
[191] L. Li, P.A. Salvador, G.S. Rohrer, Photocatalysts with internal electric fields, Nanoscale 6 (1) (2014) 24–42.
[192] F. Che, et al., Elucidating the roles of electric fields in catalysis: a perspective, ACS Catal. 8 (6) (2018) 5153–5174.
[193] L. Li, et al., Framework Cu-doped boron nitride nanobelts with enhanced internal electric field for effective Fenton-like removal of organic pollutants, J. Mater. Chem. A 7 (12) (2019) 6946–6956.
[194] Z. Gong, et al., H_2O_2 activation over Cu-Schiff bases nanozyme for the removal of amlodipine: kinetics, mechanism and toxicity evaluation, Sep. Purif. Technol. 311 (2023) 123329.
[195] T. Luo, et al., Efficient degradation of tetracycline by heterogeneous electro-Fenton process using Cu-doped Fe@ Fe_2O_3: mechanism and degradation pathway, Chem. Eng. J. 382 (2020) 122970.
[196] H. Lu, et al., Fenton-like catalysis and oxidation/adsorption performances of acetaminophen and arsenic pollutants in water on a multimetal Cu–Zn–Fe-LDH, ACS Appl. Mater. Interfaces 8 (38) (2016) 25343–25352.
[197] A. Naz, et al., Cu (II)-metalated silica-based inorganic-organic hybrid: synthesis, characterization and its evaluation for dye degradation and oxidation of organic substrates, Chem. Biochem. Eng. Q. 35 (3) (2021) 225–250.
[198] M. Gao, et al., A regenerable Cu_2O/BiOBr S-scheme heterojunction photocatalysts for efficient photocatalytic degradation of mixed organic pollutants, Sep. Purif. Technol. 313 (2023) 123447.
[199] G. Radji, et al., Heterogeneous Fenton-like degradation of organic pollutants in petroleum refinery wastewater by copper-type layered double hydroxides, J. Water Process Eng. 50 (2022) 103305.
[200] J. Tang, J. Wang, Iron-copper bimetallic metal-organic frameworks for efficient Fenton-like degradation of sulfamethoxazole under mild conditions, Chemosphere 241 (2020) 125002.
[201] Y. Sun, et al., Oxidative degradation of nitrobenzene by a Fenton-like reaction with Fe-Cu bimetallic catalysts, Appl. Catal. B 244 (2019) 1–10.
[202] S.T. Khankhasaeva, E.T. Dashinamzhilova, D.V. Dambueva, Oxidative degradation of sulfanilamide catalyzed by Fe/Cu/Al-pillared clays, Appl. Clay Sci. 146 (2017) 92–99.
[203] S. Karthikeyan, et al., Cu and Fe oxides dispersed on SBA-15: a Fenton type bimetallic catalyst for N, *N*-diethyl-p-phenyl diamine degradation, Appl. Catal. B 199 (2016) 323–330.
[204] H. Lee, et al., Chloride-enhanced oxidation of organic contaminants by Cu (II)-catalyzed Fenton-like reaction at neutral pH, J. Hazard. Mater. 344 (2018) 1174–1180.
[205] T. Ben-Moshe, I. Dror, B. Berkowitz, Oxidation of organic pollutants in aqueous solutions by nanosized copper oxide catalysts, Appl. Catal. B 85 (3–4) (2009) 207–211.

[206] M.S. Lucas, J.A. Peres, Decolorization of the azo dye reactive black 5 by Fenton and photo-Fenton oxidation, Dyes Pigments 71 (3) (2006) 236–244.
[207] L. Luo, et al., A facile strategy for enhancing FeCu bimetallic promotion for catalytic phenol oxidation, Catal. Sci. Technol. 5 (6) (2015) 3159–3165.
[208] Á. Szegedi, et al., Impact of silica structure of copper and iron-containing SBA-15 and SBA-16 materials on toluene oxidation, Microporous Mesoporous Mater. 177 (2013) 97–104.
[209] Y. Wang, H. Zhao, G. Zhao, Iron-copper bimetallic nanoparticles embedded within ordered mesoporous carbon as effective and stable heterogeneous Fenton catalyst for the degradation of organic contaminants, Appl. Catal. B 164 (2015) 396–406.
[210] J.A. Melero, et al., Nanocomposite of crystalline Fe_2O_3 and CuO particles and mesostructured SBA-15 silica as an active catalyst for wet peroxide oxidation processes, Catal. Commun. 7 (7) (2006) 478–483.
[211] Z. Han, Y. Dong, S. Dong, Copper–iron bimetal modified PAN fiber complexes as novel heterogeneous Fenton catalysts for degradation of organic dye under visible light irradiation, J. Hazard. Mater. 189 (1–2) (2011) 241–248.
[212] F. Qin, et al., Degradation of sulfamethazine by biochar-supported bimetallic oxide/persulfate system in natural water: performance and reaction mechanism, J. Hazard. Mater. 398 (2020) 122816.
[213] J. Yu, et al., Metal-free carbon materials for persulfate-based advanced oxidation process: microstructure, property and tailoring, Prog. Mater. Sci. 111 (2020) 100654.
[214] W. Yang, et al., Enhanced activation of persulfate by nitric acid/annealing modified multi-walled carbon nanotubes via non-radical process, Chemosphere 220 (2019) 514–522.
[215] X. Xia, et al., A review study on sulfate-radical-based advanced oxidation processes for domestic/industrial wastewater treatment: degradation, efficiency, and mechanism, Front. Chem. 8 (2020) 592056.
[216] K. Tian, et al., Recent advances in persulfate-based advanced oxidation processes for organic wastewater treatment, Chin. Chem. Lett. 33 (10) (2022) 4461–4477.
[217] J. Wang, et al., Treatment of refractory contaminants by sludge-derived biochar/persulfate system via both adsorption and advanced oxidation process, Chemosphere, 185 (2017) 754–763.
[218] P. Xie, et al., Impact of UV/persulfate pretreatment on the formation of disinfection byproducts during subsequent chlorination of natural organic matter, Chem. Eng. J. 269 (2015) 203–211.
[219] R. Yuan, et al., Effects of chloride ion on degradation of acid orange 7 by sulfate radical-based advanced oxidation process: implications for formation of chlorinated aromatic compounds, J. Hazard. Mater. 196 (2011) 173–179.
[220] Y.-F. Huang, Y.-H. Huang, Identification of produced powerful radicals involved in the mineralization of bisphenol A using a novel UV-$Na_2S_2O_8$/H_2O_2-Fe (II, III) two-stage oxidation process, J. Hazard. Mater. 162 (2–3) (2009) 1211–1216.
[221] C. Cai, Z. Zhang, H. Zhang, Electro-assisted heterogeneous activation of persulfate by Fe/SBA-15 for the degradation of orange II, J. Hazard. Mater. 313 (2016) 209–218.
[222] S.-Y. Oh, S.-G. Kang, P.C. Chiu, Degradation of 2, 4-dinitrotoluene by persulfate activated with zero-valent iron, Sci. Total Environ. 408 (16) (2010) 3464–3468.
[223] X. Lu, et al., Degradation of diclofenac by UV-activated persulfate process: kinetic studies, degradation pathways and toxicity assessments, Ecotoxicol. Environ. Saf. 141 (2017) 139–147.
[224] C.M. Dominguez, et al., Methanol-enhanced degradation of carbon tetrachloride by alkaline activation of persulfate: kinetic model, Sci. Total Environ. 666 (2019) 631–640.
[225] H. Milh, et al., Degradation of ciprofloxacin using UV-based advanced removal processes: comparison of persulfate-based advanced oxidation and sulfite-based advanced reduction processes, Sci. Total Environ. 764 (2021) 144510.
[226] K. Zhu, et al., In-situ formed N-doped bamboo-like carbon nanotubes encapsulated with Fe nanoparticles supported by biochar as highly efficient catalyst for activation of persulfate (PS) toward degradation of organic pollutants, Chem. Eng. J. 402 (2020) 126090.
[227] X. Xu, et al., Heterogeneous activation of persulfate by $NiFe_{2-x}Co_xO_4$-RGO for oxidative degradation of bisphenol A in water, Chem. Eng. J. 365 (2019) 259–269.
[228] S. Wacławek, et al., Chemistry of persulfates in water and wastewater treatment: a review, Chem. Eng. J. 330 (2017) 44–62.
[229] S. Xiao, et al., Iron-mediated activation of persulfate and peroxymonosulfate in both homogeneous and heterogeneous ways: a review, Chem. Eng. J. 384 (2020) 123265.
[230] J. Wang, et al., Trace Cu (II) can enhance the degradation of orange II in Fe (II)/hydroxylamine/persulfate system, J. Environ. Chem. Eng. 9 (1) (2021) 104907.
[231] Zhang, M., et al., Hydroxylamine accelerates the cycle of Fe (III)/Fe (II)-Cu (II)/Cu (I) to enhance the ability of Fe-Cu bimetallic system to activate peroxymonosulfate to degrade AO7. 2021.
[232] J. Wang, et al., Persulfate activation by copper tailings with hydroxylamine: efficiency, mechanism and DFT calculations, Sep. Purif. Technol. 297 (2022) 121472.
[233] J. Wang, et al., Facet tailoring and Cu doping promoted photo-assisted peroxymonosulfate activation by oxygen-deficient α-MnO_2 for efficient mineralization of bisphenol a, Chem. Eng. J. 461 (2023) 142024.
[234] G. Liu, et al., Efficient activation of peroxymonosulfate via Cu2+/Cu+ cycle enhanced by hydroxylamine for the degradation of Rhodamine B, Environ. Sci. Pollut. Res. 30 (12) (2023) 33133–33141.
[235] X. Liu, et al., Precise Cu localization-dependent catalytic degradation of organic pollutants in water, ChemCatChem 12 (1) (2020) 175–180.
[236] L. Wang, et al., Trace cupric species triggered decomposition of peroxymonosulfate and degradation of organic pollutants: Cu (III) being the primary and selective intermediate oxidant, Environ. Sci. Technol. 54 (7) (2020) 4686–4694.
[237] S. Wang, et al., A stable and easily prepared copper oxide catalyst for degradation of organic pollutants by peroxymonosulfate activation, J. Hazard. Mater. 387 (2020) 121995.
[238] X. Lei, et al., $CuFe_2O_4$@ GO nanocomposite as an effective and recoverable catalyst of peroxymonosulfate activation for degradation of aqueous dye pollutants, Chin. Chem. Lett. 30 (12) (2019) 2216–2220.
[239] C. Alexopoulou, et al., Copper phosphide and persulfate salt: a novel catalytic system for the degradation of aqueous phase micro-contaminants, Appl. Catal. B 244 (2019) 178–187.
[240] Y. Yang, et al., Sustainable redox processes induced by peroxymonosulfate and metal doping on amorphous manganese dioxide for nonradical degradation of water contaminants, Appl. Catal. B 286 (2021) 119903.
[241] S. Chen, et al., Simultaneous removal of para-arsanilic acid and the released inorganic arsenic species by CuFe2O4 activated peroxymonosulfate process, Sci. Total Environ. 742 (2020) 140587.
[242] J. Peng, et al., Degradation of atrazine by persulfate activation with copper sulfide (CuS): kinetics study, degradation pathways and mechanism, Chem. Eng. J. 354 (2018) 740–752.
[243] J. Lyu, et al., One-pot synthesis of magnetic CuO/Fe_2O_3/$CuFe_2O_4$ nanocomposite to activate persulfate for levofloxacin removal: investigation of efficiency, mechanism and degradation route, Chem. Eng. J. 389 (2020) 124456.
[244] L. Zhang, et al., Boric acid enhanced degradation of organic pollutant by Cu (II)/peroxymonosulfate: performance and mechanism, Sep. Purif. Technol. 293 (2022) 121135.
[245] A. Jawad, et al., Activation of persulfate by CuOx@ Co-LDH: a novel heterogeneous system for contaminant degradation with broad pH window and controlled leaching, Chem. Eng. J. 335 (2018) 548–559.
[246] H. Shan, et al., Highly flexible, mesoporous structured, and metallic Cu-doped C/SiO_2 nanofibrous membranes for efficient catalytic oxidative elimination of antibiotic pollutants, Nanoscale 11 (31) (2019) 14844–14856.
[247] Z. Shi, et al., Enhanced ferrate oxidation of organic pollutants in the presence of Cu (II) Ion, J. Hazard. Mater. 433 (2022) 128772.
[248] Y. Han, et al., Cu-doped CoOOH activates peroxymonosulfate to generate high-valent cobalt-oxo species to degrade organic pollutants in saline environments, Appl. Catal. B 340 (2024) 123224.
[249] S. Movahedian, A.R. Faraji, F. Ashouri, Enhanced PMS/O_2 activation by self-crosslinked amine-gluteraldehyde/chitosan-Cu biocomposites for efficient degradation of HEPES as biological pollutants and selective allylic oxidation of cyclohexene, New J. Chem. 47 (5) (2023) 2329–2342.
[250] L. Yang, et al., Heterogeneous activation of peroxymonosulfate by Cu+-decorated g-C_3N_4 under sunlight for degradation of organic pollutants, J. Environ. Chem. Eng. 9 (6) (2021) 106596.
[251] C. Wang, et al., Enhanced mechanism of copper doping in magnetic biochar for peroxymonosulfate activation and sulfamethoxazole degradation, J. Hazard. Mater. 458 (2023) 132002.
[252] Y. Huang, et al., Degradation of atrazine by $Zn_xCu_{1-x}Fe_2O_4$ nanomaterial-catalyzed sulfite under UV–vis light irradiation: green strategy to generate $SO_4^{\bullet-}$, Appl. Catal. B 221 (2018) 380–392.
[253] X. Dong, et al., Monodispersed $CuFe_2O_4$ nanoparticles anchored on natural kaolinite as highly efficient peroxymonosulfate catalyst for bisphenol A degradation, Appl. Catal. B 253 (2019) 206–217.
[254] Y. Yao, et al., Fe, Cu-coordinated ZIF-derived bimetal encapsulated N-doped carbon nanotube for efficient remediation of various aqueous pollutants, Chem. Eng. J. 426 (2021) 131801.
[255] T. Guo, et al., Enhanced degradation of tetracycline in water over Cu-doped hematite nanoplates by peroxymonosulfate activation under visible light irradiation, J. Hazard. Mater. 416 (2021) 125838.
[256] R. Yu, et al., Copper substituted zinc ferrite with abundant oxygen vacancies for enhanced ciprofloxacin degradation via peroxymonosulfate activation, J. Hazard. Mater. 390 (2020) 121998.
[257] Y. Huang, et al., A combined radical and non-radical oxidation processes for efficient degradation of acid orange 7 in the homogeneous Cu (II)/PMS system: important role of chloride, Environ. Sci. Pollut. Res. 28 (37) (2021) 51251–51264.
[258] P. Zhou, et al., Degradation of 2, 4-dichlorophenol by activating persulfate and peroxomonosulfate using micron or nanoscale zero-valent copper, J. Hazard. Mater. 344 (2018) 1209–1219.
[259] L. Yang, et al., One-pot preparation of poly (triazine imide) with intercalation of Cu ions: a heterogeneous catalyst for peroxymonosulfate activation to degradate organic pollutants under sunlight, Inorg. Chem. Commun. 145 (2022) 109965.
[260] T. Liu, et al., Efficient activation of peroxymonosulfate by copper supported on polyurethane foam for contaminant degradation: synergistic effect and mechanism, Chem. Eng. J. 427 (2022) 131741.
[261] Y. Zhao, et al., Recovery of CuO/C catalyst from spent anode material in battery to activate peroxymonosulfate for refractory organic contaminants degradation, J. Hazard. Mater. 420 (2021) 126552.
[262] H. Chi, et al., Efficient degradation of refractory organic contaminants by zero-valent copper/hydroxylamine/peroxymonosulfate process, Chemosphere 237 (2019) 124431.
[263] Y. Wang, et al., Natural polyphenols enhanced the Cu (II)/peroxymonosulfate (PMS) oxidation: the contribution of Cu (III) and HO•, Water Res. 186 (2020) 116326.

[264] Y. Lee, et al., Activation of peroxodisulfate and peroxymonosulfate by ultrasound with different frequencies: impact on ibuprofen removal efficient, cost estimation and energy analysis, Chem. Eng. J. 413 (2021) 127487.
[265] L. Ma, et al., Improved degradation of tetracycline by Cu-doped MIL-101(Fe) in a coupled photocatalytic and persulfate oxidation system: efficiency, mechanism, and degradation pathway, Sep. Purif. Technol. 305 (2023) 122450.
[266] X. Chen, et al., Efficient activation of persulfate by metallic sulfide mineral for the efficient removal of pesticides: performance, radical generation and mechanism, J. Clean. Prod. 421 (2023) 138521.
[267] J. Li, et al., Heterogeneous catalytic oxidation for the degradation of p-nitrophenol in aqueous solution by persulfate activated with $CuFe_2O_4$ magnetic nano-particles, Chem. Eng. J. 324 (2017) 63–73.
[268] Y. Ma, et al., Fe-Cu co-doped carbon-based catalyst activating peroxydisulfate for the degradation of tetrabromobisphenol A: the dominant role of superoxide radicals, J. Water Process Eng. 53 (2023) 103704.
[269] P. Xu, et al., Chloride ion with ferric ion in boosting zero-valent copper activated peroxydisulfate for efficiently removing tetracycline, Chem. Eng. J. 471 (2023) 144773.
[270] Y. Zhang, et al., Degradation of acetaminophen with ferrous/copperoxide activate persulfate: synergism of iron and copper, Water Res. 146 (2018) 232–243.
[271] L. Ma, et al., Improved degradation of tetracycline by Cu-doped MIL-101 (Fe) in a coupled photocatalytic and persulfate oxidation system: efficiency, mechanism, and degradation pathway, Sep. Purif. Technol. 305 (2023) 122450.
[272] Y. Liu, et al., Activation of sodium percarbonate by micro amounts of copper for highly efficient degradation of acid orange 7, Sep. Purif. Technol. 322 (2023) 124256.
[273] Y. Li, et al., Ascorbic acid-enhanced CuO/percarbonate oxidation: insights into the pH-dependent mechanism, ACS ES&T Eng. 3 (6) (2023) 798–810.
[274] S. Liu, et al., Catalytic activation of percarbonate with synthesized carrollite for efficient decomposition of bisphenol S: performance, degradation mechanism and toxicity assessment, J. Hazard. Mater. 462 (2024) 132719.
[275] D. Kiejza, et al., Peracids–New oxidants in advanced oxidation processes: the use of peracetic acid, peroxymonosulfate, and persulfate salts in the removal of organic micropollutants of emerging concern—A review, Sci. Total Environ. 790 (2021) 148195.
[276] X.-w. Ao, et al., Peracetic acid-based advanced oxidation processes for decontamination and disinfection of water: a review, Water Res. 188 (2021) 116479.
[277] L. Zhang, et al., Removal of diclofenac in water using peracetic acid activated by zero valent copper, Sep. Purif. Technol. 276 (2021) 119319.
[278] L. Zhang, et al., Highly efficient activation of peracetic acid by nano-CuO for carbamazepine degradation in wastewater: the significant role of H_2O_2 and evidence of acetylperoxy radical contribution, Water Res. 216 (2022) 118322.
[279] T. Luukkonen, U. von Gunten, Oxidation of organic micropollutant surrogate functional groups with peracetic acid activated by aqueous Co(II), Cu(II), or Ag(I) and geopolymer-supported Co(II), Water Res. 223 (2022) 118984.
[280] S.M. Patil, et al., Autocatalyzed oxidation of d-glucitol by alkaline copper (III) periodate complex: a kinetic and mechanistic approach, J. Phys. Org. Chem. 34 (3) (2021) e4146.
[281] Y.R. Sahu, P. Mishra, Kinetics and mechanism of oxidation of carbenicillin by copper (III) periodate complex in aqueous alkaline medium, J. Chem. 2020 (2020) 1–13.
[282] Y. Sukhatskiy, et al., Periodate-based advanced oxidation processes for wastewater treatment: a review, Sep. Purif. Technol. 304 (2023) 122305.
[283] A. Khataee, et al., Sonocatalytic removal of an organic dye using TiO_2/Montmorillonite nanocomposite, Ultrason. Sonochem. 22 (2015) 404–411.
[284] O. Hamdaoui, E. Naffrechoux, Sonochemical and photosonochemical degradation of 4-chlorophenol in aqueous media, Ultrason. Sonochem. 15 (6) (2008) 981–987.
[285] T.J. Mason, D. Peters, Practical Sonochemistry, 18, Elsevier, 1991.
[286] K. Suslick, The Yearbook of Science and the Future, 138, Encyclopedia Britannica, Chicago, 1994.
[287] T.J. Mason, J.P. Lorimer, Applied Sonochemistry: The Uses of Power Ultrasound in Chemistry and Processing, 10, Wiley-Vch Weinheim, 2002.
[288] L.H. Thompson, L. Doraiswamy, Sonochemistry: science and engineering, Ind. Eng. Chem. Res. 38 (4) (1999) 1215–1249.
[289] Y.G. Adewuyi, Sonochemistry: environmental science and engineering applications, Ind. Eng. Chem. Res. 40 (22) (2001) 4681–4715.
[290] M.R. Hoffmann, I. Hua, R. Höchemer, Application of ultrasonic irradiation for the degradation of chemical contaminants in water, Ultrason. Sonochem. 3 (3) (1996) S163–S172.
[291] J. Peller, O. Wiest, P.V. Kamat, Sonolysis of 2, 4-dichlorophenoxyacetic acid in aqueous solutions. Evidence for• OH-radical-mediated degradation, J. Phys. Chem. A 105 (13) (2001) 3176–3181.
[292] A. Khataee, et al., Synthesis of copper (I, II) oxides/hydrochar nanocomposites for the efficient sonocatalytic degradation of organic contaminants, J. Ind. Eng. Chem. 95 (2021) 73–82.